

HIGH-RESOLUTION NEAR-INFRARED SPECTROSCOPIC STUDY OF GALACTIC SUPERNOVA REMNANTS. I. KINEMATIC DISTANCES

YONG-HYUN LEE,^{1,2} BON-CHUL KOO,² AND JAE-JOON LEE¹

¹*Korea Astronomy and Space Science Institute, Daejeon 305-348, Korea*

²*Department of Physics and Astronomy, Seoul National University, Seoul 151-747, Korea*

ABSTRACT

We have carried out high-resolution near-infrared spectroscopic observations toward 16 Galactic supernova remnants (SNRs) showing strong H₂ emission features. A dozen bright H₂ emission lines are clearly detected for individual SNRs, and we have measured their central velocities, line widths, and fluxes. For all SNRs except one (G9.9–0.8), the H₂ line ratios are well consistent with that of thermal excitation at $T \sim 2000$ K, indicating that the H₂ emission lines are most likely from shock-excited gas and therefore that they are physically associated with the remnants. The kinematic distances to the 15 SNRs are derived from the central velocities of the H₂ lines using a Galactic rotation model. We derive for the first time the kinematic distances to four SNRs: G13.5+0.2, G16.0–0.5, G32.1–0.9, and G33.2–0.6. Among the remaining 11 SNRs, the central velocities of the H₂ emission lines for six SNRs are well consistent (± 5 km s⁻¹) with those obtained in previous radio observations, while for the other five SNRs (G18.1–0.1, G18.9–1.1, Kes 69, 3C 396, W49B) they are significantly different. We discuss the velocity discrepancies in these five SNRs. In G9.9–0.8, the H₂ emission shows nonthermal line ratios and narrow line width (~ 4 km s⁻¹), and we discuss its origin.

Keywords: Supernova Remnants (1667); Distance measure (395); Molecular clouds (1072);
High resolution spectroscopy (2096); Interstellar line emission (844)

1. INTRODUCTION

Distance is an essential and important parameter for the study of Galactic supernova remnants (SNRs), but its determination is difficult as in most areas of astronomy. Among the ~ 300 known Galactic SNRs, therefore, only a limited number of SNRs have reliable distance estimates (Green 2019).

A most popular distance determination method for SNRs is to derive the kinematic distance from velocity information using a Galactic rotation model. The classical method is to observe H I 21 cm absorption, which was introduced in the mid-1950s and was first applied to the SNR Cassiopeia A (Williams & Davies 1954; Hagen et al. 1955; see also Muller 1959). In this H I absorption technique, the absorption of 21 cm continuum from an SNR by intervening *cold* H I clouds is observed, and the maximum velocity where the absorption occurs provides a *lower and/or upper* limit to the distance to the SNR. For SNRs bright in radio, it is straightforward to apply this technique because the absorption profiles can be obtained directly from either single-dish or interferometric observations, although the noncircular motions of H I gas due to streaming along the spiral arms can hamper the derivation of accurate limits (e.g., Clark et al. 1962; Green & Gull 1989; Koo et al. 1993; Kothes et al. 2003; Kothes 2013). For SNRs faint in radio, however, it is not straightforward because, in order to obtain the absorption spectrum by an SNR, the background spectrum needs to be derived from the observation of the surrounding area and subtracted from the SNR spectrum, where the random fluctuation of H I profiles along different lines of sight could produce artificial absorption features (e.g., Green & Gull 1982). Recently, an improved method using high-resolution H I data, together with CO observation data, has been devised and systematically applied to two dozen SNRs (Leahy & Tian 2010; Ranasinghe & Leahy 2018a,b, and references therein).

For SNRs interacting with ambient molecular clouds (MCs), their kinematic distances can also be derived from the velocities of the MCs. According to the compilation by Jiang et al. (2010) and Kilpatrick et al. (2016), there are ~ 50 SNRs suggested to be interacting with MCs. The evidence for the interaction ranges from a simple morphological association to the presence or detection of shock signatures such as the broad molecular lines, the high $^{12}\text{CO } J=2-1/1-0$ line ratios, 1720 MHz OH masers, and near-infrared (NIR) rovibrational H_2 emission lines. The kinematic distances to SNRs have been derived mainly from the velocities of CO emission lines (Jiang et al. 2010; Kothes et al. 2003; Kilpatrick et al. 2016, and references

therein) or OH masers (Frail et al. 1996; Green et al. 1997; Yusef-Zadeh et al. 2003; Hewitt et al. 2008, and references therein). The studies using H₂ emission lines are relatively sparse. The H₂ 2.122 μm line had been first detected in the SNR IC 443 in 1979 (Treffers 1979), and later in several well-studied SNRs (see Lee et al. 2019 and references therein). There have, however, been neither systematic studies of SNRs in the H₂ 2.122 μm line nor spectroscopic studies to measure the distance of SNRs using the H₂ 2.122 μm line until very recently (see below). This contrasts with CO $J=1-0$ 115 GHz or OH 1720 MHz maser lines, the importance of which as a distance indicator had been realized early and for which systematic surveys toward SNRs were carried out (e.g., Huang & Thaddeus 1986; Frail et al. 1996; Green et al. 1997). The major reason for the sparseness of such studies in the H₂ 2.122 μm line might be because high-performance NIR detector arrays became available relatively recently (e.g., Rieke 2007).

Recently, we have carried out a systematic H₂-emission line study of SNRs in the inner Galaxy using the UKIRT Wide-field Infrared survey for H₂ (UWISH2; Froebrich et al. 2011), which is an unbiased survey of the inner Galactic plane ($7^\circ < l < 65^\circ$ and $|b| < 1.3^\circ$) in the H₂ 2.122 μm emission line (Lee et al. 2019). Among the 79 Galactic SNRs in the survey area, we detected a total of 19 SNRs with H₂ emission features. Comparing the H₂ and radio continuum morphologies, we suggested that the H₂ emission features are associated with the SNRs. Some H₂ emission features are found outside the [Fe II]/X-ray/radio boundaries (known as the “[Fe II]-H₂ reversal” phenomena), but their spatial distribution, together with the H₂ emission-line ratios from a follow-up NIR spectroscopy, indicates that these H₂ features are also probably associated with the SNRs (see also Section 3.1).

In this paper, we present results from high-resolution NIR spectroscopy of the H₂ emission features around the Galactic SNRs detected by Lee et al. (2019). The purpose of the study is to derive their kinematic distances by measuring accurate central velocities of H₂ lines. This paper is organized as follows. In Section 2, we describe our NIR spectroscopic observations and the data reduction procedure. In Section 3, we examine the physical association of H₂ emission with the SNRs by investigating the excitation mechanism of the H₂ emission from their line ratios and line widths. We also derive their kinematic distances from the central velocities and compare them with those of previous radio observations. In Section 4, we discuss one SNR

showing nonthermal excitation of H₂ emission lines and also five SNRs whose H₂ central velocities are significantly different from previous results. The summary of this paper is given in Section 5.

2. OBSERVATIONS AND DATA REDUCTION

2.1. Near-infrared Spectroscopy

We carried out NIR spectroscopy of H₂ emission-line features detected around the Galactic SNRs using the Immersion GRating INfrared Spectrograph (IGRINS) mounted on the Harlan J. Smith 2.7 m telescope located at McDonald Observatory. IGRINS is a high-resolution (resolving power $R \sim 45,000$) NIR spectrograph that provides simultaneous wavelength coverage of *H* and *K* band (1.5–1.8 μm and 1.9–2.5 μm , respectively; Yuk et al. 2010; Park et al. 2014). The slit width and length are 1'' and 15'', respectively.

The observations had been carried out in 2014 May, 2015 June, and 2016 July. Among the 19 H₂-emitting SNRs confirmed by Lee et al. (2019), 16 were observed (Figure 1). We carefully selected slit positions to obtain spectra of strong H₂ emission features at the border of the remnants. For several SNRs, the spectra at multiple slit positions had been obtained. The slit positions of all the targets are shown in Figure 1. The sizes of the emission features are either comparable to or larger than the slit length, so we took “OFF”-position spectra just before or after the target observations to subtract the sky-background emission/continuum. The single exposure time per frame was limited to 300 s in order to prevent saturation of the bright-sky airglow emission lines. To increase the sensitivity for weak H₂ emission-line features, however, we took multiple observations for several H₂ emission features. We also took several spectra of nearby A0V standard stars for photometric calibration.

For the data reduction, we utilized the dedicated pipeline for IGRINS written in PYTHON¹. The pipeline performs flat-fielding correction and sky subtraction at the beginning of the data reduction. Then, it performs distortion correction to produce two-dimensional spectra. Wavelength calibration was done by comparing the observed OH airglow emission lines with their vacuum wavelengths, and the overall 1σ uncertainty is about half-pixel width, which corresponds to $\sim 1 \text{ km s}^{-1}$. For photometric calibration together with telluric absorption correction, we derived the wavelength-dependent conversion factor from digital to physical units

¹ PLP version 2.2.0. The pipeline package is downloadable at <https://github.com/igrins/plp>

by comparing the observed A0V standard stars with the Kurucz model spectra², and we multiplied it by each target spectrum.

In all the spectra, we clearly detected bright H₂ 2.122 μm emission lines. Most of them show other H₂ emission lines in *H* and *K* bands too. We performed a single Gaussian fit for all the detected H₂ lines (Figure 2), except for the lines detected in four slits (G18.9–1.1-C, Kes 69-NE, and 3C 391-NE and SW), to derive their central velocities, line widths, and fluxes. For the four exceptions, the observed lines are broad and not well fitted by a single Gaussian shape (Figure 2). In such cases, we first performed fitting the H₂ 2.122 μm line with two Gaussian components, and then we applied its profile to the remaining H₂ lines to measure their fluxes. Therefore, the relative flux ratio of the two velocity components is the same for every H₂ line. All the observed central velocities have been corrected to the velocities with respect to the local standard of rest (LSR; v_{LSR}), and the observed line widths have been corrected for the instrumental broadening (7 km s⁻¹). The extinction correction for the observed line fluxes has been done by using the hydrogen column density (N_{H}) derived from previous studies (see Table 4 of Lee et al. (2019)), adopting a general interstellar extinction model with $R_V = 3.1$ (Draine 2003). For four SNRs, G9.9–0.8, G13.5+0.2, G16.0–0.5, and G33.2–0.6, however, N_{H} are not available, so we estimated the visual extinction A_V from the kinematic distance derived in this work by using the average ratio of visual extinction to path length in the solar neighborhood $\langle A_V/L \rangle \approx 1.8 \text{ mag kpc}^{-1}$ (Whittet 1992) and converted it to the NIR extinction using the extinction model of Draine (2003). The derived physical properties are listed in Table 1.

2.2. ¹²CO $J = 1-0$ Archival Data

In order to search MCs associated with the SNRs, we utilize the high-resolution ¹²CO $J = 1-0$ data from the FOREST (FOur-beam REceiver System on the 45 m Telescope) Unbiased Galactic Plane Survey with Nobeyama 45 m telescope (FUGIN; Umemoto et al. 2017), which is one of the legacy projects utilizing the new multibeam receiver FOREST. The receiver has a wide bandwidth to obtain $J = 1-0$ emission-line data of ¹²CO, ¹³CO, and C¹⁸O simultaneously. The survey was carried out from April 2014 to March 2017 to cover the first ($10^\circ < l < 50^\circ$, $|b| < 1^\circ$) and the third ($198^\circ < l < 236^\circ$; $|b| < 1^\circ$) quadrants of the Galactic

² Kurucz, R. L. 2003, <http://kurucz.harvard.edu/>

plane. The telescope has a beam size of $\sim 15''$ at 115 GHz, and the mapping was done with a sampling interval of $8''.5$. The archival data provide an effective angular resolution of $20''$ and velocity resolution of 1.3 km s^{-1} . The typical sensitivity of the ^{12}CO data is 0.24 K. The calibrated data cubes in FITS format were retrieved from the Japanese Virtual Observatory portal³ operated by the Astronomy Data Center of the National Astronomical Observatory of Japan.

3. RESULTS

3.1. Association with SNRs

The H_2 emission features in the 16 SNRs in Table 1 are “morphologically” associated with the SNRs (Lee et al. 2019). We, however, cannot rule out the chance projection of the H_2 emission features on the SNRs. In order to confirm their physical association, we investigate the excitation mechanism of the H_2 emission using H_2 line ratios. Previous NIR spectroscopic studies of several SNRs have shown that the H_2 lines excited by SNR shocks have thermal line ratios corresponding to $T \sim 2000\text{--}3000 \text{ K}$ (IC 443, Burton et al. 1988, 1989; Moorhouse et al. 1991; RCW 103, Oliva et al. 1990; Burton & Spyromilio 1993; Cygnus Loop, Graham et al. 1991; G11.2–0.3, Koo et al. 2007; Lee et al. 2019; Kes 69, Lee et al. 2019). In this paper, we use the flux ratios of $2\text{--}1 \text{ S}(1)/1\text{--}0 \text{ S}(1)$, $1\text{--}0 \text{ S}(2)/1\text{--}0 \text{ S}(0)$, and $1\text{--}0 \text{ S}(1)/1\text{--}0 \text{ S}(0)$ (Table 1) to confirm the physical association between the observed H_2 lines and the SNRs.

The flux ratio of $1\text{--}0 \text{ S}(1) 2.122 \mu\text{m}$ and $2\text{--}1 \text{ S}(1) 2.248 \mu\text{m}$ lines has been widely used to distinguish thermal and nonthermal excitation. (e.g., Burton 1992; Mouri 1994; Pak et al. 2004; Mazzalay et al. 2013; Le et al. 2017). Since these two lines originate from the same rotational state but from different vibrational states, their flux ratio is independent of the ortho-to-para ratio (OPR) that could affect the observed line ratio. For the collisionally excited emission lines from warm ($T = 2000\text{--}3000 \text{ K}$) H_2 gas, the flux ratio is in the range of 0.1–0.2 (e.g., Mouri 1994). Nonthermal excitation by UV fluorescence, on the other hand, involves the UV pumping of H_2 molecules to the excited electronic states and the cascade to the lower states, and the H_2 line ratios depend on the branching ratios in the downward cascade. This increases the populations of the high-energy levels ($v \geq 2$), which yields a flux ratio $2\text{--}1 \text{ S}(1)/1\text{--}0 \text{ S}(1)$ higher than that from the

³ <http://jvo.nao.ac.jp/portal/>

collisionally excited H_2 gas. For the pure UV fluorescence emission from the diffuse H_2 gas ($\lesssim 10^4 \text{ cm}^{-3}$) irradiated by UV photons, the $2-1 \text{ S}(1)/1-0 \text{ S}(1)$ ratio is in the range of 0.5–0.6 (Black & van Dishoeck 1987; Sternberg & Dalgarno 1989; Burton 1992). The ratios among the $\nu = 1-0$ rovibrational lines in UV fluorescence emission are also different from those in thermal emission, so that the flux ratios $1-0 \text{ S}(2)/1-0 \text{ S}(0)$ and $1-0 \text{ S}(1)/1-0 \text{ S}(0)$ are also useful to discriminate between thermal and nonthermal excitation. At higher densities, a substantial column of UV-heated, warm gas develops and the thermal emission dominates the $\nu = 1-0$ lines, but the temperature of this UV-heated thermal gas is $T \leq 1000 \text{ K}$ (Sternberg & Dalgarno 1989), substantially lower than that of the shocked gas, so that the UV-heated thermal gas is clearly separated from the shock-excited gas in the H_2 line ratio diagrams (e.g., Mouri 1994).

Figure 3 shows the distribution of H_2 line ratios of 34 positions in 16 SNRs where the abscissa is $2-1 \text{ S}(1)/1-0 \text{ S}(1)$ and the ordinate is $1-0 \text{ S}(2)/1-0 \text{ S}(0)$ or $1-0 \text{ S}(0)/1-0 \text{ S}(1)$. The solid line represents the locus of thermal emission from a source in local thermodynamic equilibrium (LTE). In the figure, we also mark the locations of nonthermal UV fluorescence emission (Black & van Dishoeck 1987) and UV-heated thermal emission (Sternberg & Dalgarno 1989). Figure 3 shows that most data points are located around the $T \sim 2000 \text{ K}$ in LTE, consistent with collisionally excited thermal emission from shocked gas. Their line ratios are significantly different from either the UV fluorescence emission or the UV-heated thermal emission. There are several positions with upper limits in $2-1 \text{ S}(1)/1-0 \text{ S}(1)$ (i.e., G11.2–0.3-N, G13.5+0.2-S, G16.0–0.5-E1 and E2, G18.1–0.1-SE, G32.1–0.9-NW and C, G33.2–0.6-W, and 3C 396-W2), but their upper limits are much smaller than that of the pure nonthermal UV fluorescence (0.50–0.60; Black & van Dishoeck 1987), and their $1-0 \text{ S}(2)/1-0 \text{ S}(0)$ and/or $1-0 \text{ S}(0)/1-0 \text{ S}(1)$ are significantly different from that of the UV-heated thermal emission. Therefore, the $1-0 \text{ S}(1) \text{ H}_2$ emission lines from those positions are also probably collisionally excited thermal emission (see below). The only exception is G9.9–0.8-NW. Its $2-1 \text{ S}(1)/1-0 \text{ S}(1)$ ratio is 0.31 ± 0.04 , which is clearly larger than that of the thermal emission at 2000 K. But the ratio is also considerably smaller than the typical line ratio of the pure UV fluorescence emission. Its $1-0 \text{ S}(0)/1-0 \text{ S}(1)$ ratio (0.49 ± 0.04) is also much larger than that of the thermal emission and is almost comparable to those of the pure nonthermal UV fluorescence (0.45–0.60; Black & van Dishoeck 1987). These line ratios suggest that the H_2 emission in G9.9–0.8-NW is likely a mixture of thermal and nonthermal

emission. It is worthwhile to note that its line width is also very small ($4.4 \pm 0.1 \text{ km s}^{-1}$) compared to the other SNRs, whose line widths are larger than 9 km s^{-1} . It is comparable to the line width ($2\text{--}6 \text{ km s}^{-1}$; Kaplan et al. 2017; Le et al. 2017; Oh et al. 2018) of nearby photodissociation regions (PDRs). We will discuss the nature of this source in Section 4.1.

One thing to note in Figure 3 is that there is a large scatter in the line ratios around the solid line representing the thermal H_2 gas in LTE conditions. This might be mostly due to the uncertainty in the $1\text{--}0 \text{ S}(0)$ and $1\text{--}0 \text{ S}(2)$ line fluxes, although it could also be partly due to the uncertainty in extinction correction. The weighted means for the line ratios are $2\text{--}1 \text{ S}(1)/1\text{--}0 \text{ S}(1) = 0.101 \pm 0.003$, $1\text{--}0 \text{ S}(2)/1\text{--}0 \text{ S}(0) = 1.98 \pm 0.03$, and $1\text{--}0 \text{ S}(0)/1\text{--}0 \text{ S}(1) = 0.188 \pm 0.003$, which agree well with the thermal emission at 2000 K. It is, however, worthwhile to note that several H_2 emission features are beyond the SNR boundary in radio: G11.2–0.3-N, S, SE, and NE; Kes 73-W; W44-N; 3C 396-W1 and W2; and W49B-E1 and E2 (Figure 1; see also Lee et al. 2019). Most of them have some morphological connection with the SNRs, i.e., they are either connected to an SNR filament (W44) or parallel to the SNR boundary (Kes 73, 3C 396, and W49B). This, together with their thermal line ratios, strongly supports their physical association with the SNRs. Their central velocities are also comparable to those of the other positions in individual SNRs (Table 1). Perhaps the only exception is G11.2–0.3. In this SNR, the H_2 emission features extend far beyond the SNR boundary and there is no obvious morphological connection between the H_2 emission features and the SNR. We can find no H II region spatially coincident with the H_2 emission in the WISE Catalog of Galactic H II regions (V2.2; Anderson et al. 2014). On the other hand, the line ratios of all four positions are consistent with the shock excitation, and their central velocities are comparable to the suggested systemic velocity of the SNR ($+45 \text{ km s}^{-1}$; Green et al. 1988), so that the association with the SNR is likely (see also Koo et al. 2007). Such H_2 filaments have been known from the early days of NIR observations, and it was pointed out that heating/exciting sources other than the SNR shock are required for the H_2 emission (Oliva et al. 1990; Graham et al. 1991; Burton & Spyromilio 1993). One possibility is the X-ray emission from SNRs; if molecular gas is irradiated by X-ray, the temperature can reach $\leq 3000 \text{ K}$ and the H_2 line ratios can be close to those of shocked gas (Lepp & McCray 1983; Draine & Woods 1990). We will explore this possibility and the origin of such H_2 emission in our forthcoming paper. In this work, we will not distinguish those

positions from the rest, which is acceptable because their velocities are comparable to those of the other positions in an SNR.

3.2. Kinematic Distances

Our analysis in Section 3.1 suggests that the observed H₂ emission features are all physically associated with the SNRs except one (G9.9–0.8). The central velocities of the H₂ 2.122 μm emission lines in Table 1, therefore, should be close to the systemic velocities of the SNRs. For the H₂ emission features in the central areas of the SNRs, however, there could be a large contribution from the shock motion to the central velocity. Indeed, in G32.1–0.9 and W44, the central velocities from the central area slits are either much ($\sim 20 \text{ km s}^{-1}$) larger (G32.1–0.9) or smaller (W44) than those from the other slits. We therefore exclude the data from the central area slits (i.e., slit name with “C” in Table 1) in deriving the systemic velocities. We also exclude the data from the slits showing two velocity components (see Figure 2), although one of the two components could represent the systemic velocity of the SNR. We then proceed to obtain the systemic velocities of the SNRs as follows: (1) For the SNRs with a single slit observation, we simply take the central velocities. (2) For the SNRs with multiple slit observations and with the spread in velocity less than 5 km s^{-1} , which is comparable to the cloud-to-cloud velocity dispersion of MCs in the inner Galaxy (e.g., see Figure 4 of Clemens 1985), we take the average of the central velocities weighted by $1/\sigma_v^2$, where σ_v is the 1σ uncertainty of the central velocity from the Gaussian fitting (Section 2.1). (3) For the SNRs with multiple slit observations and with velocity spread larger than 5 km s^{-1} , we present the range given by the minimum and maximum central velocities.

Table 2 shows the systemic velocities (v_{LSR}) of the 16 SNRs derived from our H₂ emission lines. Note that we have included SNR G9.9–0.8 in parentheses, although the association of the H₂ emission with the SNR is not certain. The table also shows the systemic velocities determined from H I absorption, CO emission, or OH maser observations in previous studies. For four SNRs (G13.5+0.2, G16.0–0.5, G32.1–0.9, and G33.2–0.6), no velocity information can be found in the literature. The left panel of Figure 4 compares the systemic velocities of 12 SNRs from our work with those from previous studies in radio ($v_{\text{LSR,radio}}$). For seven SNRs, they agree with each other within $\pm 5 \text{ km s}^{-1}$, supporting the association of all emission features with the SNRs. On the other hand, for five SNRs (G18.1–0.1, G18.9–1.1, Kes 69, 3C 396, and

W49B) the discrepancy between the two velocities is large (12–52 km s⁻¹). There could be several possible explanations. First, the H₂ emission-line velocities could have some contribution from shock motion, although it might be small because the H₂ filaments are located near the edge of the SNRs. Alternatively, the velocities obtained in previous studies, mostly from H I and/or CO observations, can be in substantial error. In Section 4, we will discuss the origin of the discrepancies in these five SNRs.

The v_{LSR} derived either from our H₂ emission lines or from radio observations can be converted to kinematic distance, adopting an appropriate Galactic rotation curve model. We use the recent model of Reid et al. (2014), which is based on ~ 100 high-mass star forming regions with accurate distances determined by trigonometric parallax. The model adopts the ‘universal’ rotation curve of Persic et al. (1996) with new Galactic parameters ($R_0 = 8.34$ kpc and $V_0 = 241$ km s⁻¹). The kinematic distances obtained by using the model of Reid et al. (2014) are listed in Table 2. For the SNRs without previous systemic velocity measurements, we present the distances estimated from other nonkinematic methods such as the Σ - D relation, where Σ and D are the radio surface brightness and the diameter of the SNRs or the Sedov analysis for comparison (see Table 2). The Sedov analysis assumes that the SNR is in the Sedov phase and has a canonical SN explosion energy of 10^{51} erg. These distance estimates can be used but have a large uncertainty. For G18.9–1.1, we also give the distance (1.8 kpc) derived from the comparison of the X-ray absorbing columns and the extinction variation to the SNR direction (Shan et al. 2018). It is worth noticing that there are two kinematic distances, near-side and far-side distances, corresponding to a v_{LSR} . For the majority of SNRs, this distance ambiguity has been resolved by H I absorption studies (see Section 1). For the SNRs without such information, we have adopted the kinematic distances close to those from the Σ - D relation or the Sedov analysis. They are marked by question marks in Column (3) of Table 2. The right panel of Figure 4 compares the distances derived from our NIR H₂ observations with those from previous studies. Not surprisingly, the five SNRs with a large discrepancy in v_{LSR} (G18.1–0.1, G18.9–1.1, Kes 69, 3C 396, and W49B) also show large distance discrepancy ($\Delta d > 1$ kpc). For the four SNRs (G13.5+0.2, G16.0–0.5, G32.1–0.9, G33.2–0.6), previous distance estimates have large uncertainties, and our result provides reliable kinematic distances for the first time, although the near-far distance ambiguity needs to be resolved for them.

4. DISCUSSION

In this section, we discuss the origin of the dense molecular gas emitting H₂ emission lines detected in the northwestern border of G9.9-0.8. We also discuss the five SNRs (G18.1–0.1, G18.9–1.1, Kes 69, 3C 396, and W49B) showing a large discrepancy in v_{LSR} between our NIR H₂ emission-line observations and the previous radio observations.

4.1. G9.9–0.8

SNR G9.9–0.8 was first identified by Brogan et al. (2006) in their VLA 90 cm observation and shows a broken shell-like morphology with a radius of 6'. Stupar & Parker (2011) detected strong H α emission features in the northwestern border of the remnant and suggested that the emission is associated with the remnant based on the positional coincidence of the bright radio continuum and the H α emission. Kilpatrick et al. (2016) detected broadened CO emission at $v_{\text{LSR}} = +27\text{--}+33 \text{ km s}^{-1}$ near the southwestern border of the remnant and obtained the kinematic distance of ~ 4 kpc assuming that the broadening is due to the interaction with the SNR.

In Lee et al. (2019), we found narrow H₂ filaments in the northwestern border of the remnant where the radio continuum is bright and optical H α emission is detected (Brogan et al. 2006; Stupar & Parker 2011). In our NIR spectroscopy of the filaments, we found very narrow H₂ emission lines (FWHM $\sim 4 \text{ km s}^{-1}$; Table 1) with nonthermal line ratios (Figure 3), indicating that they are likely arising from unshocked interstellar medium (ISM) irradiated by nearby UV sources (Section 3.1). We also check the level population diagram of the H₂ emission as shown in Figure 5. In the figure, we clearly see that the populations are not explained by thermal excitation models at temperatures of 2000–4000 K. Instead, they show “zigzag” patterns between ortho- and para-levels. We estimate the OPR of the H₂ gas using two H₂ emission lines, 1–0 S(1) and 1–0 S(0). Since the extinction-corrected 1–0 S(1)/1–0 S(0) is 2.1 ± 0.2 , assuming the rotational temperature of ~ 1700 K from 1–0 S(2)/1–0 S(0) of 1.6 ± 0.2 , the OPR of the H₂ gas is ~ 1.4 , which is much smaller than 3.0 expected in thermal H₂ gas in LTE condition. The zigzag patterns in the level population diagram, together with low OPR, seem to be consistent with typical characteristics of nonthermal UV fluorescence excitation (e.g., Hasegawa et al. 1987; Sternberg & Neufeld 1999). But, as we pointed out in

Section 3.1, the observed 2–1 S(1)/1–0 S(1) ratio (~ 0.3) is considerably smaller than that (0.6–0.7) in pure UV fluorescence excitation, suggesting that there could be some contribution from collisional excitation. The model calculations of [Draine & Bertoldi \(1996\)](#) show that warm PDRs in low-density media can yield H₂ line ratios similar to what we observe in G9.9–0.8. The solid line in Figure 5 shows the line ratios obtained in one such model (the “bh3d” model of [Draine & Bertoldi 1996](#)).

In Figure 6, we compare the spatial distribution of the H₂ emission features with that of the optical H α emission features detected in [Stupar & Parker \(2011\)](#). As seen in the figure, the H₂ filaments are detected just outside the H α emission features, and their morphologies and distributions are almost anticorrelated. The spatial distributions of the atomic and molecular emission lines suggest a PDR where UV photons from massive stars heat H₂ molecules in MCs in contact with the H II region ([Hollenbach & Tielens 1997, 1999](#)). Indeed, there is an H II region (G9.982–0.752) around the H₂ filaments (Figure 6). This H II region was identified by [Lockman \(1989\)](#), who performed a radio recombination line survey of continuum sources in the northern Galactic plane. Its location is well consistent with those of the H₂ and H α emission features, and its v_{LSR} ($=+34.4 \pm 1.5 \text{ km s}^{-1}$) is also similar to that of the H₂ emission line.

All the information described above indicates that the optical H α and NIR H₂ emission is arising from the PDR of the H II region, rather than the SNR G9.9–0.8. It is, however, worth noticing that the velocity center of the broadened CO emission ($+31 \text{ km s}^{-1}$; [Kilpatrick et al. 2016](#)) detected around the southwestern border of the remnant is very close to this velocity. If the broadened CO emission is due to the interaction of the SNR and nearby MCs as suggested by [Kilpatrick et al. \(2016\)](#), it is likely that the H II region and the SNR are located at nearly the same distance ($\sim 3.8 \text{ kpc}$; see Table 2) and that they are possibly associated. Additional observations with multi-wave-band instruments may reveal their physical connection.

4.2. G18.1–0.1

G18.1–0.1 is an SNR that belongs to the H II region/SNR complex at $l = 18^\circ 2$ and $b = -0^\circ 3$. The complex is composed of at least four H II regions and one SNR. G18.1–0.1 is located at the western edge of the complex, and it was first confirmed as an SNR by [Brogan et al. \(2006\)](#). In radio continuum, it has a broken ring-like morphology with the bright northern and eastern arcs. Although the remnant belongs to the H II region/SNR complex, their physical association is not clear (e.g., [Paron et al. 2013](#); [Leahy et al. 2014](#)).

Using ^{13}CO line data, [Paron et al. \(2013\)](#) suggested that a big molecular shell at $v_{\text{LSR}} = +51\text{--}+55 \text{ km s}^{-1}$ is physically associated with the H II region/SNR complex, placing the complex at the kinematic distance of ~ 4 kpc. For the SNR, however, [Leahy et al. \(2014\)](#) proposed a distance of ~ 6 kpc based on its H I spectrum showing absorption up to $+100 \text{ km s}^{-1}$, and argued that the remnant is located at 2–3 kpc behind of the H II regions without any physical association with them.

In [Lee et al. \(2019\)](#), we detected strong, narrow H_2 filaments at the northern and eastern borders of the remnant, where the radio continuum brightness is enhanced ([Brogan et al. 2006](#)). We also found additional diffuse H_2 emission outside of the remnant’s western boundary, but those emission features are likely associated with the nearby H II regions. We took NIR spectra of the northern and eastern borders of the remnant (Figure 1). The morphological relation with the SNR and the line ratios (Section 3.1) indicate that the H_2 emission features are associated with the remnant. The v_{LSR} of the northern filament is $+73 \text{ km s}^{-1}$, whereas that of the eastern filament is $+85 \text{ km s}^{-1}$ (Table 1). These velocities are considerably different from those of previous CO/H I results ($+53 \text{ km s}^{-1}$ or $+100 \text{ km s}^{-1}$; [Paron et al. 2013](#); [Leahy et al. 2014](#); [Ranasinghe & Leahy 2018b](#)).

In order to find MCs associated with the SNR, we have investigated high-resolution $^{12}\text{CO } J = 1\text{--}0$ data obtained as a part of the FUGIN CO survey ([Umemoto et al. 2017](#); see also Section 2.2). Figure 7 displays the $^{12}\text{CO } J = 1\text{--}0$ line channel maps between $+48$ and $+85 \text{ km s}^{-1}$. In the channel maps, the most prominent feature is the large MCs between $v_{\text{LSR}} = +48$ and $+56 \text{ km s}^{-1}$. In the middle of the velocity range, a ring-like structure emerges, which is clearly seen in the $+51 \text{ km s}^{-1}$ channel map. The ring structure appears to be encircling the remnant, with the eastern border of the remnant in contact with it. [Paron et al. \(2013\)](#) suggested that the H II region/SNR complex is located at this velocity and that they are physically associated with the MCs. But there is a large gap between the ring structure and the northwestern shell of the SNR, where the NIR H_2 emission lines are detected. The large molecular ring disappears at velocities higher than $+53 \text{ km s}^{-1}$, but instead, an additional MC filament emerges in the northeastern outer region of the remnant. The filament also seems to be in contact with the eastern and northeastern boundary of the remnant, but again its overall morphology does not match well the remnant. From $+61$ to $+72 \text{ km s}^{-1}$, on the other hand, we see a large molecular “wall” that appears to be in contact with the eastern boundary of the remnant. The

morphology is suggestive of the interaction, but the velocity of the H₂ emission in this region (+85 km s⁻¹) is considerably different from the CO emission.

At the velocities of the H₂ emission (+72 and +85 km s⁻¹), no dense MCs are visible. Instead, there are diffuse CO emission features around the remnant, some of which are spatially coincident with the remnant (Figure 7). In Figure 8, we show a close-up view of the diffuse CO emission and compare its distribution with the radio continuum and H₂ emission distributions. The diffuse CO emission is bright along the southern boundary of the SNR, where the radio continuum emission is faint. There are CO ‘clumps’ around the northwestern boundary of the SNR, but there is no clear spatial correlation between these CO clumps and the northwestern H₂ filament. At the eastern boundary of the remnant, we see a faint CO filament that appears to be spatially coincident with the radio/H₂ filament, but the CO emission is complex in this area and their association is not clear.

To summarize, we could not identify CO clouds clearly associated with the H₂ filaments (and the SNR). The large molecular shell at $v_{\text{LSR}} = +51\text{--}+55$ km s⁻¹ has been proposed to be associated with the SNR (Paron et al. 2013), but its velocity is very different from that of the H₂ filaments, and there is no spatial correlation between the two. Instead, we have detected diffuse CO emission features spatially coincident with the SNR at the velocities of the H₂ filaments (+72–+85 km s⁻¹). Their association is possible, although there is no clear spatial correlation between the CO and H₂ emission features. The kinematic distance corresponding to the H₂ emission-line velocities (+73–+85 km s⁻¹) is 5.0–5.5 kpc (Table 2) assuming the near-side distance.

4.3. G18.9–1.1

G18.9–1.1 belongs to the composite-type SNR with a size larger than a half degree. Early radio observations showed weak, diffuse radio continuum filling inside the remnant, together with two strong pillar-like features at the center and near the western border (e.g., Fürst et al. 1985, 1989, 1997). X-ray observations found a point-like hard X-ray source with an associated diffuse nebula at the tip of the central radio pillar, and it was suggested that these objects are a pulsar and its wind nebula (Harrus et al. 2004; Tüllmann et al. 2010). Fürst et al. (1989) reported the detection of H I depression at +18 km s⁻¹ toward the remnant and suggested that the depression is caused by a cavity associated with the remnant (see below). The v_{LSR} of +18 km s⁻¹ corresponds to the kinematic distance of either ~ 2 kpc within the Sagittarius Arm or ~ 15 kpc

on the far side of the tangential point. The latter, however, was ruled out because in that case the SNR should have very unusual properties (e.g, huge explosion energy of $(1-2)\times 10^{52}$ erg; [Fürst et al. 1989](#); [Har-rus et al. 2004](#)). A recent NIR study using the red clump stars toward the remnant suggested the distance of 1.8 ± 0.2 kpc ([Shan et al. 2018](#)), which is consistent with the above kinematic distance.

In [Lee et al. \(2019\)](#), we detected weak, patchy H_2 emission inside the remnant. Most of the H_2 emission, which has a complex morphology, arises from the central and northeastern regions, $3'-10'$ apart from the central radio pillar. Additional weak, patchy H_2 emission features were also detected in the western border of the remnant. We obtained two NIR spectra: one at the H_2 filament close to the central radio pillar, and the other at the H_2 clump near the northeastern border (Figure 1). The central velocity of the latter is $+70 \text{ km s}^{-1}$, while the spectrum of the former is composed of two velocity components centered at $+74$ and $+53 \text{ km s}^{-1}$, respectively (Table 1; see also Figure 2). If we adopt the central velocity of the northeastern H_2 clump as the systemic velocity of the SNR, the kinematic distance to the SNR would be 4.7 kpc (Table 2). But this v_{LSR} is more than 50 km s^{-1} larger than that ($+18 \text{ km s}^{-1}$) suggested by [Fürst et al. \(1989\)](#), and the distance is ~ 3 kpc larger than those (~ 2 kpc) obtained in the previous radio and NIR studies ([Fürst et al. 1989](#); [Shan et al. 2018](#)).

The large velocity difference in v_{LSR} between our H_2 emission and the previous H I absorption could be due to the peculiar velocity of the H_2 gas accelerated by the SN shock along the line of sight. However, the systemic velocity ($v_{\text{LSR}} = +70 \text{ km s}^{-1}$) is taken from the northeastern H_2 clump near the SNR boundary, so the peculiar line-of-sight velocity by the SN shock might not be large. Furthermore, the velocity difference of 50 km s^{-1} seems to be rather large for a nondissociative shock (e.g., [Draine & McKee 1993](#)). Therefore, it is possible that the v_{LSR} of the H_2 emission lines traces the systematic velocity of the remnant. Another possibility is that these central and northeastern H_2 emission features are not physically associated with the SNR, even though they are located inside the remnant (Figure 1). We searched the WISE Catalog of Galactic H II Regions (V2.2; [Anderson et al. 2014](#)) and the HASH Planetary Nebulae Database⁴ (V4.6; [Parker et al. 2016](#)) to find sources responsible for the H_2 emission, but we could not find any candidate.

⁴ The University of Hong Kong/Australian Astronomical Observatory/Strasbourg Observatory $H\alpha$ Planetary Nebula Database

In order to explore the large discrepancies in v_{LSR} and distance between our H_2 and previous results, we examined the H I absorption toward the SNR using the VLA Galactic Plane Survey (VGPS) H I data (Stil et al. 2006). The VGPS survey has an angular resolution of $1'$, which is much higher than that ($6'$) of the previous study (Fürst et al. 1989). We first extracted H I spectra toward the two central radio pillars and compared them with the spectra of the surrounding regions, but we could not identify clear absorption features because of the random fluctuations in the foreground/background H I emission. We then looked at individual channel maps and confirmed the depression at $v_{\text{LSR}} \sim +18 \text{ km s}^{-1}$ (Figure 9). The depression has a very good morphological correlation with radio continuum, e.g., there is a filamentary depression along the radio pillars, suggesting that the depression is probably due to absorption rather than a cavity as proposed by Fürst et al. (1989). We could not find absorption features at higher velocities, but the nondetection of absorption does not rule out the possibility that the SNR is at a greater distance because there is a large background fluctuation due to the nonuniform structure of the H I gas along the line of sight. The H I absorption at $+18 \text{ km s}^{-1}$ indicates that the SNR is at a distance *greater* than $\sim 2 \text{ kpc}$. The distance $1.8 \pm 0.2 \text{ kpc}$ of Shan et al. (2018) has been obtained by comparing the X-ray absorbing hydrogen column density ($(8.3 \pm 0.5) \times 10^{21} \text{ cm}^{-2}$; Harrus et al. 2004) to the extinction-distance relation derived by using red clump stars. Harrus et al. (2004), however, obtained an extinction $A_V = 5.1 \text{ mag}$, which is 1 mag greater than the value of 4.1 mag from Shan et al. (2018). And the extinction-distance relation of Shan et al. (2018) shows that A_V is almost constant at $\sim 5.2 \text{ mag}$ beyond 2 kpc. (They derived the relation up to 2.8 kpc.) Therefore, we consider that the distance 2 kpc obtained in previous studies is a minimum distance, and the distance to G18.9–1.1 is still uncertain. Future spectroscopic studies of the H_2 emission features detected in the western radio shell (Lee et al. 2019) might be helpful to clarify the issue.

4.4. *G21.8–0.6 (Kes 69)*

Kes 69 is a shell-type SNR, showing a bright incomplete radio shell along the southeastern border of the remnant. H I absorption is seen up to $+85 \text{ km s}^{-1}$ with no absorption lines around the tangential velocity ($\sim +110 \text{ km s}^{-1}$), indicating that the remnant is located on the near side of the tangential point (Tian & Leahy 2008; Zhou et al. 2009). The kinematic distance of the SNR corresponding to $+85 \text{ km s}^{-1}$ is 5.2 kpc (see Ranasinghe & Leahy 2018a). Zhou et al. (2009) showed that a molecular arc at $+77$ – $+86 \text{ km s}^{-1}$ is

morphologically correlated with the southeastern radio shell. [Hewitt et al. \(2008\)](#) detected extended faint OH 1720 MHz maser emission at $v_{\text{LSR}} = +85 \text{ km s}^{-1}$ toward the brightest portion of the southeastern radio shell. A compact OH (1720 MHz) maser spot was also detected in the northeastern region of the remnant, but at $v_{\text{LSR}} = +69.3 \text{ km s}^{-1}$ ([Green et al. 1997](#)).

In [Lee et al. \(2019\)](#), we reported the detection of an extended bright H_2 emission feature composed of multiple narrow filaments in the southeastern border of the remnant along the bright radio shell. We also detected additional complex H_2 emission features in the northeastern region of the remnant, where the OH maser has been detected ([Green et al. 1997](#)). We took NIR spectra at three positions: two in the southeastern shell and one in the northeastern region (Table 1). The v_{LSR} of the H_2 emission in the southeastern shell is $+60 \text{ km s}^{-1}$, and it is consistent with the previous NIR spectroscopy with medium resolution for the southeastern shell ($+57 \pm 3 \text{ km s}^{-1}$; [Lee et al. 2019](#)). Interestingly, this velocity is almost 30 km s^{-1} smaller than the v_{LSR} of the molecular arc detected in CO and OH maser emission ($+85 \text{ km s}^{-1}$; [Hewitt et al. 2008](#); [Zhou et al. 2009](#)). The large velocity difference is difficult to understand because the H_2 filaments are located at the border of the remnant, so that the expansion velocity of H_2 gas along the line of sight might be small.

We have investigated the presence of MCs associated with the remnant at the velocity of the H_2 emission using the FUGIN $^{12}\text{CO } J = 1-0$ data. Figure 10 shows CO channel maps at velocities from $+57$ to $+93 \text{ km s}^{-1}$, where we see that the most prominent MCs are at $+78$ – $+88 \text{ km s}^{-1}$. As shown by [Zhou et al. \(2009\)](#), the MCs in this velocity range have some morphological correlation with the SNR. In particular, the filamentary MC in the southeastern area at $\sim +80 \text{ km s}^{-1}$ correlates well with the remnant’s bright southeastern radio continuum shell. There is also extended OH maser emission with a broad line width at $+85 \text{ km s}^{-1}$ along the radio shell ([Hewitt et al. 2008](#)). At lower velocities, the CO emission is relatively faint with some large, extended CO clouds inside and around the SNR. At the velocity of the H_2 emission ($\sim +61 \text{ km s}^{-1}$), we can see a faint, clumpy MC that appears to be in contact with the southern SNR boundary (Figure 11). It has a thin, extended filamentary structure parallel to the H_2 filament in the southeastern shell, but the overall morphological correlation between the MC and the radio shell is relatively weak.

If the MCs at $+78$ – $+88$ km s $^{-1}$ in Figure 10 are associated with the SNR, as has been suggested in previous molecular line studies, the kinematic distance to Kes 69 is 5.2 kpc, adopting $+85$ km s $^{-1}$ as its systemic velocity (Hewitt et al. 2008; Zhou et al. 2009). The H $_2$ emission with a central velocity of $+61$ km s $^{-1}$, then indicates that the MC is on the front side of the SNR and that a ~ 24 km s $^{-1}$ shock is propagating into the MC. On the other hand, if the central velocity of the H $_2$ emission ($+61$ km s $^{-1}$) represents the systemic velocity of the SNR, the faint CO cloud in Figure 11 is possibly interacting with the SNR, and the association of the extended OH maser emission detected by Hewitt et al. (2008) becomes unclear. The kinematic distance corresponding to the systemic velocity of $+61$ km s $^{-1}$ is 4.1 kpc. Future spectral mapping of the H $_2$ emission might be helpful to resolve the issue.

4.5. *G39.2–0.3 (3C 396)*

3C 396 is a composite-type SNR exhibiting both a central X-ray pulsar wind nebula (PWN) and an incomplete radio shell composed of multiple filaments (Harrus & Slane 1999). Previous H I and OH absorption studies suggested that the remnant is located on the far side of the tangential point at $v_{\text{LSR}} \lesssim +60$ km s $^{-1}$ (Caswell et al. 1975; see also Green 1989). The remnant is believed to be interacting with MCs in the west, where the bright radio shell and NIR H $_2$ filaments are detected. According to CO observations, there are two large MCs that could be possibly associated with the remnant: one at $+69$ km s $^{-1}$ and the other at $+84$ km s $^{-1}$. Lee et al. (2009) found MCs at $v_{\text{LSR}} = +68$ – $+70$ km s $^{-1}$ surrounding the remnant and pointed out that the western H $_2$ filament is in contact with the inner boundary of the MCs. Kilpatrick et al. (2016) also suggested the association of these MCs with the SNR. On the other hand, Su et al. (2011) found a thick molecular wall at $+84$ km s $^{-1}$ in the western border of the remnant with high $^{12}\text{CO } J=2-1/J=1-0$ line ratios and suggested that the SNR is interacting with these MCs.

Previous NIR H $_2$ narrowband imaging observations had detected two long H $_2$ filaments aligned along the north-south direction, leaving an interval of $\sim 1'.5$ in the western region of the remnant (Lee et al. 2009, 2019). The brighter filament is located near the western edge of the remnant, slightly outside the radio boundary of the SNR. Lee et al. (2009) attributed the H $_2$ filaments to the interaction between the SNR and nearby MCs at $+69$ km s $^{-1}$. Our NIR spectroscopy toward the two locations in the filament shows that v_{LSR} of the filament is $+56$ km s $^{-1}$ (Table 1). This is consistent with the result of an early H I absorption study

(Caswell et al. 1975), but it is considerably (by 10–20 km s⁻¹) smaller than those inferred from previous CO observations (+69, +84 km s⁻¹; Lee et al. 2009; Su et al. 2011; Kilpatrick et al. 2016).

In Figure 12, we revisit the ¹²CO $J = 1-0$ channel maps from +52 to +91 km s⁻¹ to find the molecular features associated with the remnant. The most prominent feature are the large MCs at velocities from +52 to +70 km s⁻¹ in the northern and western regions of the remnant. At +52 km s⁻¹, these large MCs appear in the western region, 2'–4' apart from the remnant boundary. They move to the central area of the field at higher velocities, so that at $\sim +57$ km s⁻¹ they are almost in contact with the remnant boundary. Around +54–+57 km s⁻¹, we also see extended MCs in the eastern region of the remnant, which seems to be in contact with the eastern boundary of the remnant. From +62 to +70 km s⁻¹, large MCs appear in the northern region. A couple of MC filaments extend from the northern MCs toward the south, and one of them at +70 km s⁻¹ is almost in contact with the SNR along the southwestern boundary of the remnant. Lee et al. (2009) suggested that this MC filament is physically associated with the remnant. At velocities $> +72$ km s⁻¹, we see relatively diffuse, extended MCs around the remnant, which disappear at velocities higher than the tangential velocity ($\sim +85$ km s⁻¹). In particular, at +85 km s⁻¹, we see several clouds superposed on the bright western radio shell. Su et al. (2011) found high ¹²CO $J=2-1/J=1-0$ line ratios at the velocity channel and suggested that these CO clouds are interacting with the remnant.

Figure 13 shows the zoomed-in ¹²CO channel map of 3C 396 at +56 km s⁻¹, which is the central velocity of the H₂ emission lines. An interesting thing is that the remnant is located inside a cavity surrounded by MCs. The western half of the cavity is prominent, and its inner boundary appears to be parallel to the SNR boundary. Except the northwestern region, there is a $\sim 2'$ gap between the remnant boundary and the cavity wall. But there is a filamentary cloud spatially coincident with the H₂ filament inside the cavity. The eastern half of the cavity is surrounded by relatively faint MCs. The SNR radio emission is faint in this area, but the SNR appears to be in contact with the cavity wall along the southeastern boundary of the SNR.

As we have shown in Figure 12, there are at least three possible MCs at velocities +56, +69, and +84 km s⁻¹, respectively, that could be associated with the SNR (see also Lee et al. 2009; Su et al. 2011; Kilpatrick et al. 2016). They all have some morphological relation with the SNR. At the velocity of the H₂ emission, i.e., at +56 km s⁻¹, we see a CO cavity surrounding the SNR and a faint filamentary MC spatially

coincident with the bright western shell. Therefore, the MCs at $+56 \text{ km s}^{-1}$ are very likely to be associated with the SNR. The cavity surrounding the SNR could be a wind bubble produced by the progenitor. The SNR is on the far side (Caswell et al. 1975), so that the kinematic distance corresponding to $+56 \text{ km s}^{-1}$ is 9.5 kpc.

4.6. *G43.3–0.2 (W49B)*

W49B is a member of the W49 complex that includes multiple H II regions (W49A) and one SNR (W49B). Previous H I 21 cm observations toward the W49 complex showed that the absorption is seen up to the tangential velocity ($\sim +70 \text{ km s}^{-1}$) at positive velocities, but not at negative velocities (Lockhart & Goss 1978; Brogan & Troland 2001; Zhu et al. 2014; Ranasinghe & Leahy 2018b). This indicates that the sources in the W49 complex are located beyond the tangential point but inside the solar circle. There have been many efforts to reveal the relative distances to W49A and W49B and the physical association between them. In H I and H₂CO absorption spectra, it was found that there is an absorption at $\sim +10 \text{ km s}^{-1}$ toward W49A that is not seen toward W49B (Kazes 1970; Wilson 1970; Radhakrishnan et al. 1972). This suggests that W49A is most likely located at the far distance (11.5 kpc), corresponding to $+10 \text{ km s}^{-1}$ and that W49B is in front of W49A without any physical association between them (Kazes 1970; Wilson 1970; Radhakrishnan et al. 1972). This distance to W49A was later confirmed by the comparison of proper motions of the H₂CO masers and their Doppler velocities ($11.4 \pm 1.2 \text{ kpc}$; Gwinn et al. 1992). The early H I and H₂CO absorption studies suggested that W49B is located at $\sim 8 \text{ kpc}$ (Moffett & Reynolds 1994) corresponding to the maximum velocity of the absorption lines ($+63 \text{ km s}^{-1}$; Kazes 1970; Wilson 1970; Radhakrishnan et al. 1972). Brogan & Troland (2001), however, suggested that the different absorption velocities between W49A and W49B could be due to the differences of H I kinematics, distribution, and temperature in the direction of W49 complex and that one cannot rule out the physical association between them. Another distance estimate for W49B is from CO observations. Toward W49B, there are three large MCs at different v_{LSR} : $+10$, $+40$, and $+60 \text{ km s}^{-1}$ (Zhu et al. 2014; Kilpatrick et al. 2016). Zhu et al. (2014) argued that the MCs at $+40 \text{ km s}^{-1}$ are morphologically associated with the remnant and suggested a distance of $\sim 10 \text{ kpc}$. Kilpatrick et al. (2016), on the other hand, reported the detection of broadened ¹²CO emission centered

at $v_{\text{LSR}} = +14 \text{ km s}^{-1}$ in the southwestern boundary of the remnant and suggested 11.3 kpc, although the physical association between the remnant and the MCs is not clear.

In Lee et al. (2019), we found bright H_2 emission features in the eastern and western areas of the remnant. In the eastern area, we see several narrow, extended filaments along the NE-SW direction outside the X-ray/[Fe II]/radio boundary. In the western area, on the other hand, the H_2 emission features are rather clumpy and mostly detected inside the remnant. There are also some additional H_2 filaments aligned along the NE-SW direction in the central area of the remnant, but they are much fainter than those in the eastern and western areas. The morphology and the H_2 line ratios (Section 3.1) indicate that the bright H_2 emission features in the east and west areas (and probably the faint filaments in the central area too) are thermally excited and physically associated with the remnant. We obtained NIR spectra at four positions: two for the eastern filaments, and one for each of the northern and the western H_2 emission features (Figure 1). We found that their v_{LSR} are $\sim +64 \text{ km s}^{-1}$ without any significant variations (only $\pm 2 \text{ km s}^{-1}$), and this led us to conclude that the systematic velocity of the remnant is $+64 \text{ km s}^{-1}$. Our result is consistent with the suggestions by the early HI and H_2CO absorption studies (Kazes 1970; Wilson 1970; Radhakrishnan et al. 1972), but is very different from those of previous CO observations, i.e., $+10$ or $+40 \text{ km s}^{-1}$ (Zhu et al. 2014; Kilpatrick et al. 2016). The kinematic distance corresponding to $+64 \text{ km s}^{-1}$ is 7.5 kpc (Table 2).

We revisit ^{12}CO channel maps to confirm the MC(s) associated with the SNR. Figure 14 shows the ^{12}CO $J = 1-0$ channel maps toward W49B in three different velocity ranges where the large MCs are located (Zhu et al. 2014; Kilpatrick et al. 2016): (1) $+7-+17 \text{ km s}^{-1}$, (2) $+38-+48 \text{ km s}^{-1}$, and (3) $+59-+69 \text{ km s}^{-1}$. In the velocity range from $+7$ to $+17 \text{ km s}^{-1}$, there are two large prominent MCs, i.e., an extended filamentary MC in the northern area of the field and a large MC outside the western boundary of the SNR. There is diffuse CO emission spread over the SNR that appears to be extended from these two MCs. There is no clear overall morphological correlation between the diffuse emission and the H_2 emission. But at $+14 \text{ km s}^{-1}$, there is a $\sim 4'$ -long filamentary CO cloud along the southwestern boundary of the SNR that appears to surround the H_2 -bright area. Kilpatrick et al. (2016) found broadened CO emission lines toward this cloud suggesting the association of the MC with the SNR. The presence of the H_2 emission further supports the SNR-MC interaction, but the large ($\sim 50 \text{ km s}^{-1}$) velocity difference between the H_2 and the CO emission

is difficult to reconcile. In the velocity range from $+38 \text{ km s}^{-1}$ to $+48 \text{ km s}^{-1}$, there are diffuse CO clouds around the remnant. As pointed out by [Zhu et al. \(2014\)](#), the MCs appear to surround the SNR (see also Figure 1 of [Chen et al. 2014](#)). In particular, at $+43 \text{ km s}^{-1}$, there are MCs just outside the eastern and southwestern H_2 -bright regions. If these MCs are interacting with the SNR, the velocity of the H_2 emission ($+64 \text{ km s}^{-1}$) implies that the MCs are on the backside of the SNR. In the velocity range $+59$ – $+69 \text{ km s}^{-1}$, the CO emission is complex with several velocity components. Note that this is the velocity range where HI and H_2CO absorption is prominent, especially toward the southwestern area of the SNR ([Bieging et al. 1982](#); [Brogan & Troland 2001](#); see also [Lacey et al. 2001](#)). Toward the southwestern H_2 -bright region, there are at least two velocity components at $+61$ and $+66 \text{ km s}^{-1}$, respectively. The $+61 \text{ km s}^{-1}$ component is part of the large MC aligned along the northeast-southwest direction crossing the remnant’s center. At this velocity, we also see a relatively faint CO filament outside the eastern SNR boundary that appears to be aligned with the eastern H_2 -bright region (see next paragraph). The $+66 \text{ km s}^{-1}$ component seems to be part of the large MC cloud in the western area of the field, which partly overlaps with the southwestern H_2 -bright region. There is also some faint CO emission at this velocity just outside the eastern H_2 -bright region, but only in its southern area.

Figure 15 is a zoomed-in ^{12}CO channel map integrated from $+61$ to $+66 \text{ km s}^{-1}$, where we found the H_2 emission lines. Note that the color scale is changed from that in Figure 14. The figure shows that the $+61 \text{ km s}^{-1}$ MC crossing the SNR has a “tuning-fork” morphology with the U-shaped prongs in the interior. The left prong runs along the northeast-southwest direction, spatially coincident with one of the radio filaments in the interior, while the western prong is located just inside the western radio shell, where the radio continuum is bright and the H_2 emission lines are detected. In the eastern area, along the extended H_2 -bright region, there are faint MCs that appear, blocking the H_2 region. These MCs are aligned with the tuning-fork MC but with a gap between them. There is also diffuse emission spread over the field, including the areas around the southwestern H_2 -bright region.

As we have shown in Figure 14, the CO emission toward W49B is complicated, and it is difficult to identify MCs associated with the SNR based on their morphology. Instead, the roughly constant central velocities of the H_2 emission over the SNR suggest that the systemic velocity of the SNR is probably

$\sim +64 \text{ km s}^{-1}$. We therefore consider that the MCs at $+59$ – $+69 \text{ km s}^{-1}$ are associated with the SNR. In particular, the MCs at $+61$ – $+66 \text{ km s}^{-1}$ seem to have a good morphological correlation with the SNR (Figure 15). The interaction of the SNR with these MCs aligned along the northeast-southwest direction could have resulted in the barrel-like morphology of the SNR. The kinematic distance 7.5 kpc corresponding to $+64 \text{ km s}^{-1}$ is $\sim 4 \text{ kpc}$ closer than W49A ($11.4 \pm 1.2 \text{ kpc}$; Gwinn et al. 1992).

5. SUMMARY

Distance is a basic parameter of the Galactic SNRs and is essential for deriving their physical parameters, such as radius, luminosity, age, and explosion energy. Diverse methods have been devised, each of which has its own strengths and weaknesses. A popular method is to identify an object associated with the SNR and derive the kinematic distance from its LSR velocity. This technique has been most widely used in radio by using the CO emission from MCs or OH maser emission. In this paper, we have shown that the NIR H_2 emission, which is a strong signature of the interaction between SNRs and MCs, can also be used for the distance determination. We performed high-resolution NIR spectroscopy for 16 SNRs detected in our systematic H_2 emission-line study of SNRs in the inner Galaxy (Lee et al. 2019). In all SNRs, bright H_2 1–0 S(1) $2.122 \mu\text{m}$ emission lines, together with additional H_2 emission lines from different excitation levels, were clearly detected. We examined the excitation mechanism of the H_2 emission lines in order to confirm their physical association with the SNRs, and we derived the kinematic distances of SNRs from the central velocities of the H_2 lines. For four SNRs, the kinematic distances have been determined in this work for the first time.

The comparison showed that the central velocities of H_2 emission lines are considerably ($> 5 \text{ km s}^{-1}$) different from those obtained from radio observations for five SNRs: G18.1–0.1, G18.9–1.1, Kes 69, 3C 396, and W49B. Since the detection of collisionally excited H_2 emission in an SNR is strong evidence that the SNR is interacting with an MC, we consider that the H_2 central velocities and the inferred kinematic distances should be preferred to those based on morphological association if there is a large discrepancy. However, as pointed out in Section 3.2, the kinematic distance from the H_2 line, with the matter of their physical association put aside, also has its inherent uncertainties. Firstly, the measured velocity is that of the shocked gas, not the ambient gas. Secondly, the H_2 emission samples a highly localized region within

an MC, so that the velocity may represent the outskirts of cloud velocity distribution rather than the central velocity of the cloud. More detailed studies are needed to fully accept the H₂ line-based distances for these five SNRs.

Our main results are summarized in the following:

1. In all SNRs, except G9.9–0.8, the H₂ lines show thermal line ratios with $T \sim 2000$ K, indicating that they are emitted from warm, collisionally excited H₂ gas. The thermal line ratios support that most, if not all, H₂ emission features are associated with the SNRs.

2. We have derived the kinematic distances of 16 SNRs (including G9.9–0.8) by using the velocities of the H₂ emission lines (see below for the discussion about G9.9–0.8). For four SNRs (G13.5+0.2, G16.0–0.5, G32.1–0.9, and G33.2–0.6), the kinematic distances have been determined in this work for the first time. For 6 out of the remaining 11 SNRs, v_{LSR} derived from our H₂ emission lines are well consistent ($< \pm 5$ km s⁻¹) with those from previous radio observations, which provides a support to the derived kinematic distances. For five SNRs, however, there is a large discrepancy between the two velocities, which casts doubt on the derived kinematic distances.

3. For five SNRs showing large discrepancy in v_{LSR} between our H₂ and the previous radio observations (G18.1–0.1, G18.9–1.1, Kes 69, 3C 396, W49B), we have explored the origin of the discrepancy using CO and H I data. The results on individual SNRs are summarized below.

(1) G18.1–0.1: The velocities of the two extended H₂ filaments along the northern and eastern radio boundaries have been measured as +73 and +85 km s⁻¹, respectively. These velocities are very different from those suggested from previous CO (+51–+55 km s⁻¹; [Paron et al. 2013](#)) and H I (+100 km s⁻¹; [Leahy et al. 2014](#); [Ranasinghe & Leahy 2018b](#)) observations. At the velocities of the H₂ emission, there are some diffuse CO emission features spatially coincident with the remnant. Their association is possible. The near-side kinematic distance corresponding to the H₂ emission line velocities is 5.0–5.5 kpc.

(2) G18.9–1.1: The velocities of two short H₂ filaments have been measured: one near the northeastern boundary (+70 km s⁻¹), and the other in the central area (+74 and +53 km s⁻¹; see [Figure 2](#)). The near-side kinematic distance corresponding to +70 km s⁻¹ is 4.7 kpc. These are much greater than those suggested in previous H I (+18 km s⁻¹; [Fürst et al. 1989](#)) and red clump star (1.8 kpc [Shan et al. 2018](#)) studies. The

discrepancy may indicate that either the H₂ filaments have a large peculiar velocity or they are not associated with the SNR. The ISM structure along this line of sight, however, appears complicated, and the previous velocity/distance estimates could be lower limits.

(3) Kes 69: The velocity of the H₂ filament in the southeastern bright radio shell has been measured as +60 km s⁻¹. This is much smaller than the value of +85 km s⁻¹ of the molecular arc suggested to be interacting with the SNR from CO and OH maser emission (+85 km s⁻¹; [Hewitt et al. 2008](#); [Tian & Leahy 2008](#); [Zhou et al. 2009](#)). At the velocity of the H₂ emission, however, we see a faint, clumpy MC that could be responsible for the H₂ emission. If this +61 km s⁻¹ MC is interacting with the SNR, the near-side kinematic distance becomes 4.1 kpc.

(4) 3C 396: The velocity of the bright H₂ filament coincident with the western radio shell has been measured as +57 km s⁻¹. This velocity is considerably smaller than those suggested from previous CO observations, i.e., +69 km s⁻¹ ([Lee et al. 2009](#); [Kilpatrick et al. 2016](#)) and +84 km s⁻¹ ([Su et al. 2011](#)). We have found that, at +56 km s⁻¹, there are MCs spatially well correlated with the SNR: a CO cavity surrounding the SNR and a faint filamentary MC spatially coincident with the bright western shell. If the MCs at +56 km s⁻¹ are associated with the SNR, the kinematic distance to 3C 396, which is on the far side ([Caswell et al. 1975](#)), becomes 9.5 kpc.

(5) W49B: The velocities of the bright H₂ filaments in the the eastern and western SNR shells have been measured as \sim +64 km s⁻¹. This velocity is very different from those suggested from CO observations, i.e., +40 km s⁻¹ ([Zhu et al. 2014](#)) and +14 km s⁻¹ ([Kilpatrick et al. 2016](#)). The roughly constant velocity of the H₂ emission over the SNR suggests that the systemic velocity of the SNR is probably \sim +64 km s⁻¹. At +61–+66 km s⁻¹, we have found MCs that appear to have a good morphological correlation with the barrel-like morphology of the SNR. Adopting +64 km s⁻¹ as the systemic velocity of the SNR, the kinematic distance to W49B, which is on the far side ([Lockhart & Goss 1978](#); [Brogan & Troland 2001](#); [Zhu et al. 2014](#); [Ranasinghe & Leahy 2018b](#)), becomes 7.5 kpc.

4. For G9.9–0.8, the nonthermal lines ratios and the narrow line widths indicate that the H₂ lines are probably excited by UV radiation. The H₂ emission is most likely arising from a PDR surrounding the H II region (G9.982–0.752), rather than the SNR. However, the central velocity of the H₂ line (+30 km s⁻¹)

is almost identical to the systematic velocity of the remnant estimated from previous CO observations ($+31 \text{ km s}^{-1}$; Kilpatrick et al. 2016), suggesting the possible physical association between the H II region and the SNR.

Y.-H.L. acknowledges support from the National Research Foundation of Korea (NRF) grant funded by the Ministry of Science and ICT (MSIT) of Korea (NRF-2018M1A3A3A02065645). The work of B.-C.K. was supported by the Basic Science Research Program through the National Research Foundation of Korea (NRF) funded by the Ministry of Science, ICT and future Planning (2020R1A2B5B01001994). This work used the Immersion Grating Infrared Spectrograph (IGRINS) that was developed under a collaboration between the University of Texas at Austin and the Korea Astronomy and Space Science Institute (KASI) with the financial support of the US National Science Foundation under grant AST-1229522, the University of Texas at Austin, and the Korean GMT Project of KASI. This paper includes data taken at the McDonald Observatory of the University of Texas at Austin. This publication also makes use of data from FUGIN, the FOREST Unbiased Galactic plane Imaging survey with the Nobeyama 45 m telescope, a legacy project in the Nobeyama 45 m radio telescope. The 45 m radio telescope is operated by the Nobeyama Radio Observatory, a branch of the National Astronomical Observatory of Japan.

REFERENCES

- Anderson, L. D., Bania, T. M., Balser, D. S., et al. 2014, *ApJS*, 212, 1
- Bieging, J. H., Wilson, T. L., & Downes, D. 1982, *A&AS*, 49, 607
- Black, J. H., & van Dishoeck, E. F. 1987, *ApJ*, 322, 412
- Brogan, C. L., Gelfand, J. D., Gaensler, B. M., Kassim, N. E., & Lazio, T. J. W. 2006, *ApJL*, 639, L25
- Brogan, C. L., & Troland, T. H. 2001, *ApJ*, 550, 799
- Burton, M., & Spyromilio, J. 1993, *Proceedings of the Astronomical Society of Australia*, 10, 327
- Burton, M. G. 1992, *Australian Journal of Physics*, 45, 463
- Burton, M. G., Brand, P. W. J. L., Geballe, T. R., & Webster, A. S. 1989, *MNRAS*, 236, 409
- Burton, M. G., Geballe, T. R., Brand, P. W. J. L., & Webster, A. S. 1988, *MNRAS*, 231, 617
- Caswell, J. L., Murray, J. D., Roger, R. S., Cole, D. J., & Cooke, D. J. 1975, *A&A*, 45, 239
- Chen, Y., Jiang, B., Zhou, P., et al. 2014, in *IAU Symposium, Vol. 296, Supernova Environmental Impacts*, ed. A. Ray & R. A. McCray, 170

- Clark, B. G., Radhakrishnan, V., & Wilson, R. W. 1962, *ApJ*, 135, 151
- Claussen, M. J., Frail, D. A., Goss, W. M., & Gaume, R. A. 1997, *ApJ*, 489, 143
- Clemens, D. P. 1985, *ApJ*, 295, 422
- Draine, B. T. 2003, *ARA&A*, 41, 241
- Draine, B. T., & Bertoldi, F. 1996, *ApJ*, 468, 269
- Draine, B. T., & McKee, C. F. 1993, *ARA&A*, 31, 373
- Draine, B. T., & Woods, D. T. 1990, *ApJ*, 363, 464
- Folgheraiter, E. L., Warwick, R. S., Watson, M. G., & Koyama, K. 1997, *MNRAS*, 292, 365
- Frail, D. A., Goss, W. M., Reynoso, E. M., et al. 1996, *AJ*, 111, 1651
- Froebrich, D., Davis, C. J., Ioannidis, G., et al. 2011, *MNRAS*, 413, 480
- Fürst, E., Hummel, E., Reich, W., et al. 1989, *A&A*, 209, 361
- Fürst, E., Reich, W., & Aschenbach, B. 1997, *A&A*, 319, 655
- Fürst, E., Reich, W., Reich, P., Sofue, Y., & Handa, T. 1985, *Nature*, 314, 720
- Graham, J. R., Wright, G. S., Hester, J. J., & Longmore, A. J. 1991, *AJ*, 101, 175
- Green, A. J., Frail, D. A., Goss, W. M., & Otrupcek, R. 1997, *AJ*, 114, 2058
- Green, D. A. 1989, *MNRAS*, 238, 737
- . 2019, *Journal of Astrophysics and Astronomy*, 40, 36
- Green, D. A., & Gull, S. F. 1982, *Nature*, 299, 606
- . 1989, *MNRAS*, 237, 555
- Green, D. A., Gull, S. F., Tan, S. M., & Simon, A. J. B. 1988, *MNRAS*, 231, 735
- Gwinn, C. R., Moran, J. M., & Reid, M. J. 1992, *ApJ*, 393, 149
- Hagen, J. P., Lilley, A. E., & McClain, E. F. 1955, *ApJ*, 122, 361
- Harrus, I. M., & Slane, P. O. 1999, *ApJ*, 516, 811
- Harrus, I. M., Slane, P. O., Hughes, J. P., & Plucinsky, P. P. 2004, *ApJ*, 603, 152
- Hasegawa, T., Gatley, I., Garden, R. P., et al. 1987, *ApJL*, 318, L77
- Helfand, D. J., Becker, R. H., White, R. L., Fallon, A., & Tuttle, S. 2006, *AJ*, 131, 2525
- Hewitt, J. W., Yusef-Zadeh, F., & Wardle, M. 2008, *ApJ*, 683, 189
- Hollenbach, D. J., & Tielens, A. G. G. M. 1997, *ARA&A*, 35, 179
- . 1999, *Reviews of Modern Physics*, 71, 173
- Huang, Y. L., & Thaddeus, P. 1986, *ApJ*, 309, 804
- Jiang, B., Chen, Y., Wang, J., et al. 2010, *ApJ*, 712, 1147
- Junkes, N., Fuerst, E., & Reich, W. 1992, *A&AS*, 96, 1
- Kaplan, K. F., Dinerstein, H. L., Oh, H., et al. 2017, *ApJ*, 838, 152
- Kazes, I. 1970, *A&A*, 4, 111
- Kilpatrick, C. D., Bieging, J. H., & Rieke, G. H. 2016, *ApJ*, 816, 1
- Koo, B.-C., Moon, D.-S., Lee, H.-G., Lee, J.-J., & Matthews, K. 2007, *ApJ*, 657, 308
- Koo, B.-C., Yun, M.-S., Ho, P. T. P., & Lee, Y. 1993, *ApJ*, 417, 196
- Koralesky, B., Frail, D. A., Goss, W. M., Claussen, M. J., & Green, A. J. 1998, *AJ*, 116, 1323
- Kothes, R. 2013, *A&A*, 560, A18

- Kothes, R., Reich, W., Foster, T., & Byun, D.-Y. 2003, *ApJ*, 588, 852
- Lacey, C. K., Lazio, T. J. W., Kassim, N. E., et al. 2001, *ApJ*, 559, 954
- Le, H. A. N., Pak, S., Kaplan, K., et al. 2017, *ApJ*, 841, 13
- Leahy, D., Green, K., & Tian, W. 2014, *MNRAS*, 438, 1813
- Leahy, D., & Tian, W. 2010, in *Astronomical Society of the Pacific Conference Series*, Vol. 438, *The Dynamic Interstellar Medium: A Celebration of the Canadian Galactic Plane Survey*, ed. R. Kothes, T. L. Landecker, & A. G. Willis, 365
- Lee, H.-G., Moon, D.-S., Koo, B.-C., Lee, J.-J., & Matthews, K. 2009, *ApJ*, 691, 1042
- Lee, Y.-H., Koo, B.-C., Lee, J.-J., Burton, M. G., & Ryder, S. 2019, *AJ*, 157, 123
- Lepp, S., & McCray, R. 1983, *ApJ*, 269, 560
- Lockhart, I. A., & Goss, W. M. 1978, *A&A*, 67, 355
- Lockman, F. J. 1989, *ApJS*, 71, 469
- Mazzalay, X., Saglia, R. P., Erwin, P., et al. 2013, *MNRAS*, 428, 2389
- Moffett, D. A., & Reynolds, S. P. 1994, *ApJ*, 437, 705
- Moorhouse, A., Brand, P. W. J. L., Geballe, T. R., & Burton, M. G. 1991, *MNRAS*, 253, 662
- Mouri, H. 1994, *ApJ*, 427, 777
- Muller, C. A. 1959, in *IAU Symposium*, Vol. 9, *URSI Symp. 1: Paris Symposium on Radio Astronomy*, ed. R. N. Bracewell, 360
- Oh, H., Pyo, T.-S., Koo, B.-C., et al. 2018, *ApJ*, 858, 23
- Oliva, E., Moorwood, A. F. M., & Danziger, I. J. 1990, *A&A*, 240, 453
- Pak, S., Jaffe, D. T., Stacey, G. J., et al. 2004, *ApJ*, 609, 692
- Park, C., Jaffe, D. T., Yuk, I.-S., et al. 2014, in *Proc. SPIE*, Vol. 9147, *Ground-based and Airborne Instrumentation for Astronomy V*, 91471D
- Parker, Q. A., Bojčić, I. S., & Frew, D. J. 2016, in *Journal of Physics Conference Series*, Vol. 728, *Journal of Physics Conference Series*, 032008
- Parker, Q. A., Phillipps, S., Pierce, M. J., et al. 2005, *MNRAS*, 362, 689
- Paron, S., Weidmann, W., Ortega, M. E., Albacete Colombo, J. F., & Pichel, A. 2013, *MNRAS*, 433, 1619
- Pavlovic, M. Z., Dobardzic, A., Vukotic, B., & Urosevic, D. 2014, *Serbian Astronomical Journal*, 189, 25
- Persic, M., Salucci, P., & Stel, F. 1996, *MNRAS*, 281, 27
- Radhakrishnan, V., Goss, W. M., Murray, J. D., & Brooks, J. W. 1972, *ApJS*, 24, 49
- Ranasinghe, S., & Leahy, D. A. 2017, *ApJ*, 843, 119
- . 2018a, *MNRAS*, 477, 2243
- . 2018b, *AJ*, 155, 204
- Reid, M. J., Menten, K. M., Brunthaler, A., et al. 2014, *ApJ*, 783, 130
- Rieke, G. H. 2007, *ARA&A*, 45, 77
- Shan, S. S., Zhu, H., Tian, W. W., et al. 2018, *ApJS*, 238, 35
- Sternberg, A., & Dalgarno, A. 1989, *ApJ*, 338, 197
- Sternberg, A., & Neufeld, D. A. 1999, *ApJ*, 516, 371
- Stil, J. M., Taylor, A. R., Dickey, J. M., et al. 2006, *AJ*, 132, 1158

- Stupar, M., & Parker, Q. A. 2011, *MNRAS*, 414, 2282
- Su, Y., Chen, Y., Yang, J., et al. 2011, *ApJ*, 727, 43
- Tian, W. W., & Leahy, D. A. 2008, *MNRAS*, 391, L54
- Treffers, R. R. 1979, *ApJL*, 233, L17
- Tüllmann, R., Plucinsky, P. P., Gaetz, T. J., et al. 2010, *ApJ*, 720, 848
- Umemoto, T., Minamidani, T., Kuno, N., et al. 2017, *PASJ*, 69, 78
- Whittet, D. C. B. 1992, Dust in the galactic environment
- Williams, D. R. W., & Davies, R. D. 1954, *Nature*, 173, 1182
- Wilson, T. L. 1970, *Astrophys. Lett.*, 7, 95
- Yuk, I.-S., Jaffe, D. T., Barnes, S., et al. 2010, in *Proc. SPIE*, Vol. 7735, *Ground-based and Airborne Instrumentation for Astronomy III*, 77351M
- Yusef-Zadeh, F., Wardle, M., Rho, J., & Sakano, M. 2003, *ApJ*, 585, 319
- Zhou, P., & Chen, Y. 2011, *ApJ*, 743, 4
- Zhou, X., Chen, Y., Su, Y., & Yang, J. 2009, *ApJ*, 691, 516
- Zhu, H., Tian, W. W., & Zuo, P. 2014, *ApJ*, 793, 95

Table 1. Properties of H₂ Lines

SNR	Slit	Slit Position		v_{LSR} (km s ⁻¹)	FWHM (km s ⁻¹)	$\frac{2-1 S(1)}{1-0 S(1)}$	$\frac{1-0 S(2)}{1-0 S(0)}$	$\frac{1-0 S(0)}{1-0 S(1)}$
		[α (J2000) δ (J2000)]	(6)			(7)	(8)	
(1)	(2)	(3)		(4)	(5)	(6)	(7)	(8)
G9.9-0.8	NW	18:10:26.33	-20:39:41.9	+30.4 (0.1)	4.4 (0.1)	0.31 (0.04)	1.62 (0.19)	0.49 (0.04)
G11.2-0.3	N	18:11:26.64	-19:21:52.2	+47.3 (0.2)	12.6 (0.4)	<0.16	<15.2	0.18 (0.04)
	S	18:11:28.85	-19:27:51.5	+46.5 (0.1)	13.2 (0.3)	0.11 (0.03)	<5.54	0.15 (0.02)
	SE	18:11:32.35	-19:27:12.0	+49.2 (0.1)	12.0 (0.1)	0.12 (0.01)	2.30 (0.07)	0.17 (0.01)
	NE	18:11:34.82	-19:23:43.0	+48.9 (0.1)	11.4 (0.1)	0.07 (0.02)	2.84 (0.47)	0.16 (0.01)
G13.5+0.2	S	18:14:20.85	-17:13:57.4	+40.1 (0.9)	32.8 (2.1)	<0.28	1.67 (1.02)	0.13 (0.05)
G16.0-0.5	E1	18:22:13.88	-15:18:15.9	+50.0 (0.3)	17.5 (0.8)	<0.18	2.30 (0.94)	0.20 (0.06)
	E2	18:22:16.47	-15:16:27.5	+52.7 (0.4)	17.1 (0.8)	<0.11	1.61 (0.54)	0.19 (0.05)
G18.1-0.1	NW	18:24:29.08	-13:10:20.7	+73.1 (0.4)	26.6 (0.8)	0.09 (0.05)	1.60 (0.40)	0.19 (0.04)
	SE	18:24:49.55	-13:12:25.9	+85.3 (0.2)	13.5 (0.4)	<0.09	1.99 (0.53)	0.20 (0.04)
G18.9-1.1	C (p) ^a	18:29:31.05	-12:51:23.7	+74.0 (1.1)	26.0 (2.2)	0.13 (0.05)	2.26 (0.78)	0.18 (0.06)
	C (s) ^a	-	-	+53.3 (1.1)	12.0 (2.1)	-	-	-
	NE	18:30:04.44	-12:51:43.0	+69.7 (0.5)	40.7 (1.3)	0.15 (0.06)	2.71 (0.80)	0.16 (0.04)
Kes 69	SE1	18:33:01.92	-10:13:43.6	+59.0 (0.4)	40.7 (1.0)	0.16 (0.03)	1.70 (0.39)	0.19 (0.03)
	SE2	18:33:14.96	-10:12:12.8	+61.7 (0.3)	28.5 (0.7)	0.15 (0.03)	1.62 (0.30)	0.23 (0.04)
	NE (p) ^a	18:33:10.12	-10:00:52.0	+77.0 (0.8)	28.8 (1.6)	0.12 (0.05)	2.51 (0.91)	0.18 (0.06)
	NE (s) ^a	-	-	+33.4 (6.6)	43.9 (15.2)	-	-	-
Kes 73	W	18:41:12.15	-04:56:42.6	+99.4 (0.1)	10.9 (0.2)	0.09 (0.02)	2.24 (0.34)	0.18 (0.02)
3C 391	NW	18:49:16.00	-00:55:04.4	+99.7 (0.8)	53.3 (2.1)	0.11 (0.04)	2.66 (1.00)	0.13 (0.04)
	NE (p) ^a	18:49:27.86	-00:55:01.4	+96.4 (0.4)	29.2 (1.8)	0.09 (0.02)	2.13 (0.29)	0.19 (0.04)
	NE (s) ^a	-	-	+76.2 (4.7)	50.6 (4.0)	-	-	-
	SW (p) ^a	18:49:23.26	-00:57:41.0	+107.0 (0.1)	25.4 (0.4)	0.09 (0.01)	1.96 (0.11)	0.20 (0.01)
	SW (s) ^a	-	-	+84.0 (1.0)	58.0 (1.1)	-	-	-
G32.1-0.9	NW	18:52:40.73	-00:56:57.4	+84.5 (0.2)	18.5 (0.5)	<0.10	1.74 (0.45)	0.22 (0.05)
	C	18:53:42.22	-01:02:01.8	+100.4 (0.1)	10.7 (0.2)	<0.07	1.95 (0.32)	0.21 (0.03)

Table 1 continued on next page

Table 1 (*continued*)

SNR	Slit	Slit Position		v_{LSR} (km s^{-1})	FWHM (km s^{-1})	$\frac{2-1 S(1)}{1-0 S(1)}$	$\frac{1-0 S(2)}{1-0 S(0)}$	$\frac{1-0 S(0)}{1-0 S(1)}$
		[α (J2000)	δ (J2000)]			(6)	(7)	(8)
(1)	(2)	(3)		(4)	(5)	(6)	(7)	(8)
Kes 78	E	18:51:46.34	-00:11:27.7	+89.5 (0.2)	22.4 (0.4)	0.11 (0.03)	2.10 (0.34)	0.19 (0.03)
G33.2-0.6	W	18:53:25.70	+00:01:09.4	+81.7 (0.5)	26.4 (1.2)	<0.17	2.26 (0.79)	0.20 (0.06)
W44	W	18:55:17.10	+01:21:50.0	+46.2 (0.1)	38.4 (0.1)	0.10 (0.01)	1.84 (0.04)	0.21 (0.01)
	N	18:55:39.80	+01:37:56.4	+41.2 (0.1)	17.3 (0.3)	0.14 (0.02)	2.04 (0.25)	0.24 (0.02)
	C	18:56:14.70	+01:20:52.7	+26.7 (0.2)	20.0 (0.4)	0.06 (0.04)	1.61 (0.32)	0.24 (0.03)
	S	18:56:35.46	+01:06:44.1	+48.9 (0.1)	24.7 (0.3)	0.16 (0.02)	1.82 (0.25)	0.20 (0.02)
3C 396	W1	19:03:55.86	+05:25:36.9	+55.9 (0.1)	10.6 (0.2)	0.08 (0.02)	<5.83	0.23 (0.02)
	W2	19:03:56.94	+05:24:38.3	+57.5 (0.3)	11.9 (0.5)	<0.10	<13.9	0.13 (0.04)
W49B	E1	19:11:16.14	+09:05:04.9	+65.5 (0.1)	8.7 (0.1)	0.07 (0.01)	2.44 (0.24)	0.18 (0.01)
	E2	19:11:16.91	+09:06:17.5	+64.3 (0.1)	9.2 (0.1)	0.10 (0.01)	2.19 (0.17)	0.18 (0.01)
	W	19:11:00.15	+09:05:07.9	+61.7 (0.1)	25.7 (0.2)	0.11 (0.01)	2.41 (0.16)	0.20 (0.01)
	N	19:11:06.46	+09:06:47.9	+64.1 (0.1)	9.3 (0.3)	0.08 (0.03)	1.95 (0.49)	0.18 (0.04)
HC 40	NW	19:32:14.18	+19:07:31.4	+44.2 (0.4)	23.6 (0.9)	0.12 (0.05)	<3.08	0.19 (0.05)

NOTE— Column (1): SNR name. Column (2): slit name. Column (3): central coordinate of the slit. Column (4): central velocity of the H_2 1-0 S(1) 2.122 μm line in the LSR frame. The uncertainties in parentheses are formal 1σ statistical errors. The uncertainty in absolute wavelength calibration is about 1 km s^{-1} . Column (5): FWHM of the H_2 1-0 S(1) lines corrected for the instrument broadening (7 km s^{-1}). Columns (6)–(8): extinction-corrected flux ratios (see text). The numbers in parentheses are 1σ errors, whereas the numbers with “<” are 3σ upper limits.

^a The H_2 line profiles are fitted by two Gaussian components: primary (p) and secondary (s). See Figure 2 and the explanation in Section 2.1.

Table 2. Kinematic Distances of 16 Galactic SNRs

SNR	Literature					H ₂	
	v_{LSR} (km s ⁻¹)	KDA	d (kpc)	Method	Reference	v_{LSR} (km s ⁻¹)	d (kpc)
(1)	(2)	(3)	(4)	(5)	(6)	(7)	(8)
G9.9-0.8	+31	N?	3.8	CO, Σ - D	1	+30 (± 1) ^a	3.8 (± 0.1) ^a
G11.2-0.3	+45	N	4.6	H I	2	+48 (± 2)	4.7 (± 0.1)
G13.5+0.2	...	F?	13 \pm 7	Σ - D	3	+40 (± 1)	12.4 (± 0.1)
G16.0-0.5	...	N?	8 \pm 4	Σ - D	3	+51 (± 2)	4.1 (± 0.1)
G18.1-0.1	+53, +100	N	4.0, 6.2	H I, CO	4, 5, 6	+73-+85	5.0-5.5
G18.9-1.1	+18	N	1.7-1.8 ^b	H I, RCS	7, 8	+70 (± 1)	4.7 (± 0.1)
Kes 69	+85	N	5.2	H I, CO, OH	9, 10, 11	+61 (± 2)	4.1 (± 0.1)
Kes 73	+100	N	5.9	H I, CO	1, 6	+99 (± 1)	5.8 (± 0.1)
3C 391	+100-+110	TP	7.1	H I, CO, OH	1, 12, 13	+100 (± 1)	7.1 (± 0.1)
G32.1-0.9	...	N?	4.6	Sedov	14	+85 (± 1)	5.0 (± 0.1)
Kes 78	+82-+86	N	4.9-5.1	H I, CO, OH	6, 15, 16	+90 (± 1)	5.4 (± 0.1)
G33.2-0.6	...	N?	6 \pm 3	Σ - D	3	+82 (± 1)	4.9 (± 0.1)
W44	+42-+50	N	2.6-3.1	H I, OH	6, 17, 18	+41-+49	2.6-3.0
3C 396	+69, +84	F	8.6, 6.8	H I, CO	6, 19, 20	+56 (± 2)	9.5 (± 0.1)
W49B	+13, +40	F	11.3, 9.6	H I, CO	1, 6, 21	+64 (± 2)	7.5 (± 0.2)
HC 40	+36-+44	F	5.4-6.8	H I, CO	13, 22	+44 (± 1)	5.4 (± 0.1)

Table 2 continued on next page

Table 2 (*continued*)

SNR	Literature					H ₂	
	v_{LSR}	KDA	d	Method	Reference	v_{LSR}	d
	(km s ⁻¹)		(kpc)			(km s ⁻¹)	(kpc)
(1)	(2)	(3)	(4)	(5)	(6)	(7)	(8)

NOTE— Column (1): SNR name. Column (2): systemic velocity of SNR from the literature. Column (3): kinematic distance ambiguity, indicating whether the SNR is at the near (N), far (F), or tangent point (TP) distance. Those with “?” indicate that the distance ambiguity had not been resolved in previous H I absorption studies and that we have adopted either near or far distance based on other studies (see text). Column (4): kinematic distance derived from the systemic velocity in Column (2). For those without the velocity information, we list the distances from other methods listed in Column (5). Column (5): distance estimation method: H I absorption (H I), CO emission (CO), Σ - D relation (Σ - D), Sedov analysis (Sedov), and red clump star (RCS) method (see text). Column (6): references for the systemic velocity or the distance. Column (7): systemic velocity of the SNR derived from the central velocities of the H₂ lines. The numbers in the parentheses are 1σ uncertainties, which are obtained by adding the absolute wavelength calibration uncertainty (1 km s⁻¹) and the standard deviation of the central velocities in quadrature. For the SNRs with multiple slit observations and with velocity spread larger than 5 km s⁻¹, the minimum and maximum central velocities are given (see Section 3.2). Column (8): kinematic distance derived from the systemic velocity in Column (7).

^a The H₂ emission is most likely arising from a PDR, and its association with the SNR is not clear (see Section 4.1).

^b 1.7 kpc is from H I absorption, and 1.8 kpc is from the RCS method.

References— (1) Kilpatrick et al. 2016; (2) Green et al. 1988; (3) Pavlovic et al. 2014; (4) Paron et al. 2013; (5) Leahy et al. 2014; (6) Ranasinghe & Leahy 2018b; (7) Fürst et al. 1989; (8) Shan et al. 2018; (9) Hewitt et al. 2008; (10) Tian & Leahy 2008; (11) Zhou et al. 2009; (12) Frail et al. 1996; (13) Ranasinghe & Leahy 2017; (14) Folgheraiter et al. 1997; (15) Koralesky et al. 1998; (16) Zhou & Chen 2011; (17) Caswell et al. 1975; (18) Claussen et al. 1997; (19) Lee et al. 2009; (20) Su et al. 2011; (21) Zhu et al. 2014; (22) Junkes et al. 1992.

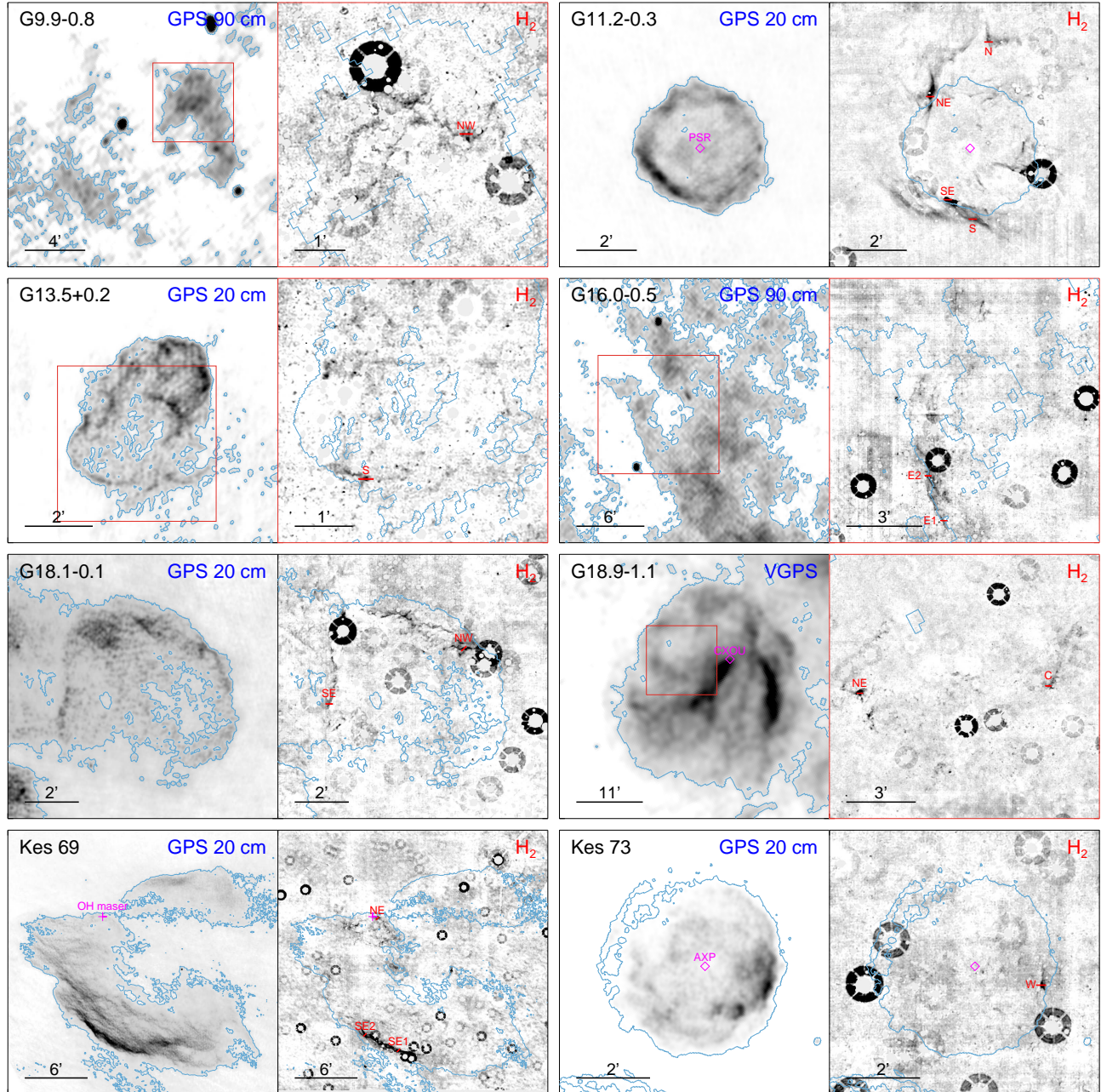


Figure 1. Radio and H_2 $2.122 \mu\text{m}$ narrowband images of the 16 SNRs studied in this paper. North is up, and east is to the left. The radio images are from either the VLA 20/90 cm Galactic Plane Survey (GPS 20/90cm; Helfand et al. 2006) or the VLA 21 cm Galactic Plane Survey (VGPS; Stil et al. 2006), while the H_2 images are from Lee et al. (2019). The gray scales are linear, and the blue contours represent the SNR boundary in radio continuum. In the radio images, the red box marks the boundary of the H_2 image of the source and the magenta symbols represent the locations of X-ray/radio sources associated with the SNR: crosses = OH masers; open diamonds = pulsars or point-like X-ray sources. The slit positions for the NIR spectroscopy are marked on the H_2 images (red bars). The slit names represent the directions from the SNR's center to the slits (i.e., N, S, E, and W indicate north, south, east, and west, respectively, whereas C indicates the central area inside the SNR boundary).

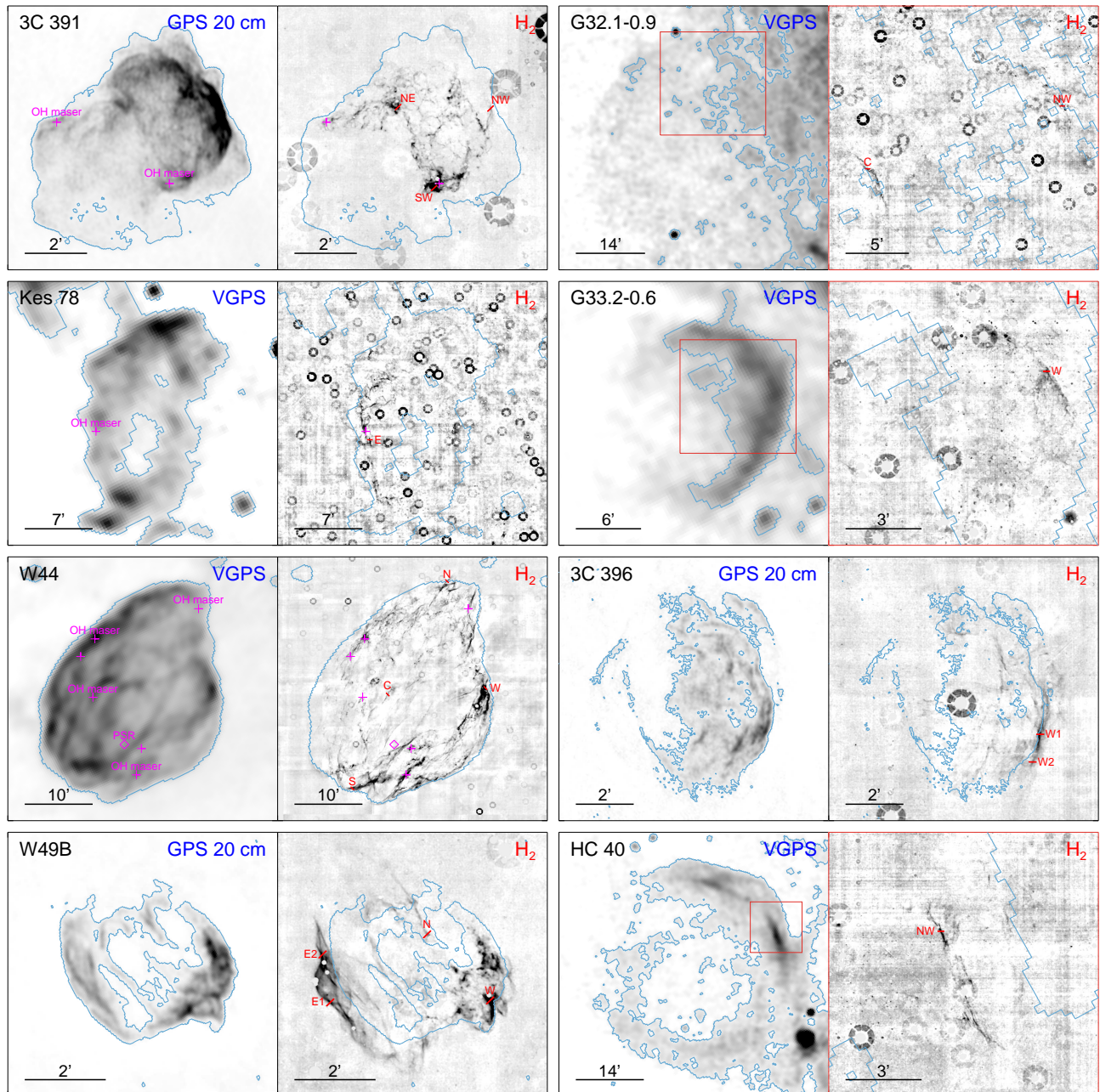


Figure 1. (Continued)

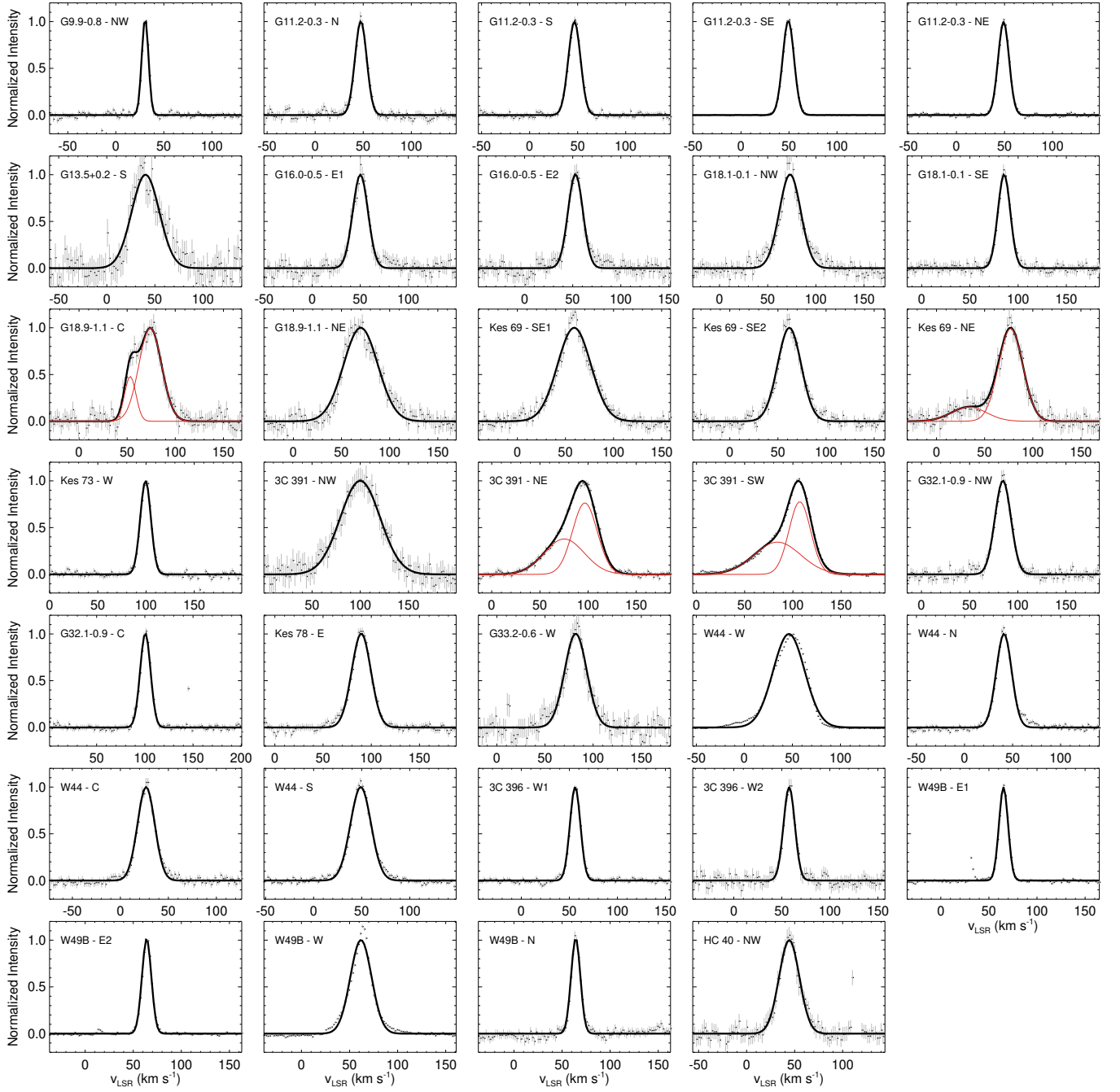


Figure 2. H_2 1–0 S(1) 2.122 μm spectra of the 34 targets in Table 1. The gray dots with vertical bars represent the observed spectra with 1σ uncertainties, while the black solid lines are the model profiles resulting from Gaussian fittings. For four targets, G18.9–1.1-C, Kes 69-NE, 3C 391-NE, and 3C 391-SW, the spectra are fitted by two Gaussian components (see Section 2.1), and each component is shown by a red solid line.

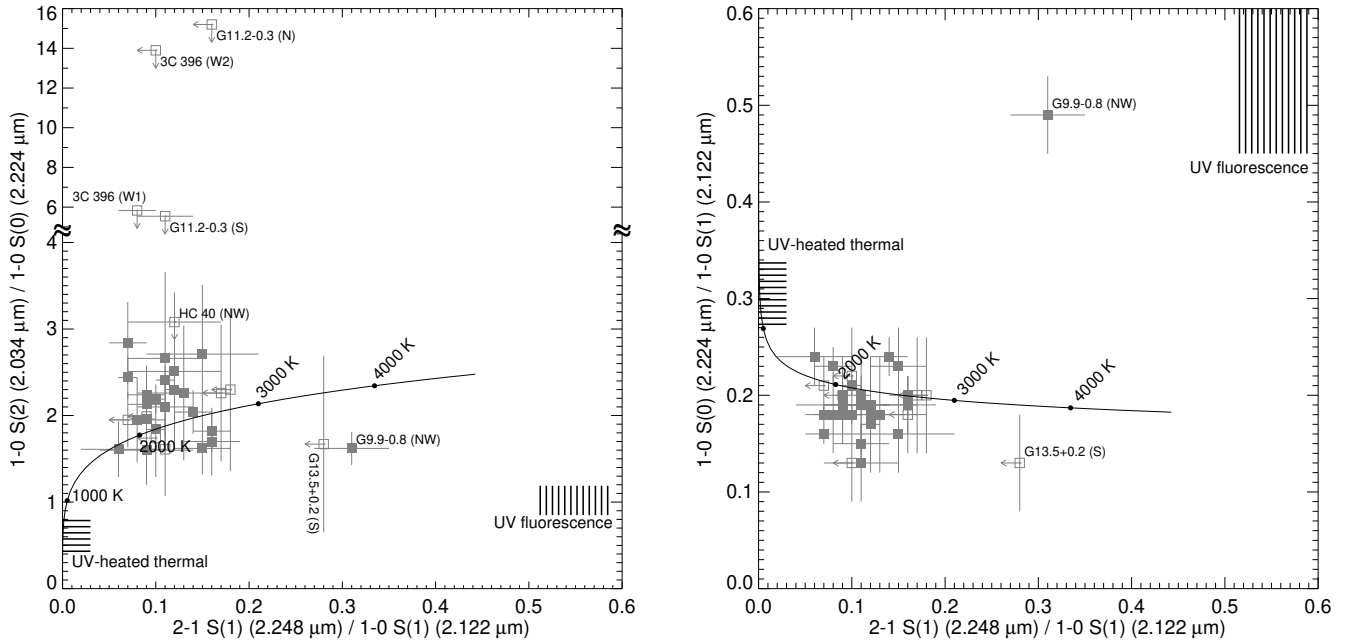


Figure 3. Flux ratios of H_2 emission lines: $2-1\ S(1)\ (2.248\ \mu\text{m}) / 1-0\ S(1)\ (2.122\ \mu\text{m})$ vs. $1-0\ S(2)\ (2.034\ \mu\text{m}) / 1-0\ S(0)\ (2.224\ \mu\text{m})$ (left), and $2-1\ S(1)\ (2.248\ \mu\text{m}) / 1-0\ S(1)\ (2.122\ \mu\text{m})$ vs. $1-0\ S(0)\ (2.224\ \mu\text{m}) / 1-0\ S(1)\ (2.122\ \mu\text{m})$ (right). The filled squares represent the extinction-corrected flux ratios of 34 targets (Table 1), while the open squares with arrows indicate the 3σ upper limits of the ratios. The black solid line represents the flux ratios of thermal gas in LTE at $T = 1000\text{--}4000\ \text{K}$. The vertical and horizontal stripes indicate the areas of the diagram corresponding to nonthermal UV fluorescence (Black & van Dishoeck 1987) and UV-heated thermal excitation models (Sternberg & Dalgarno 1989), respectively. Note that the y-axis of the left panel has a discontinuity at ~ 5 .

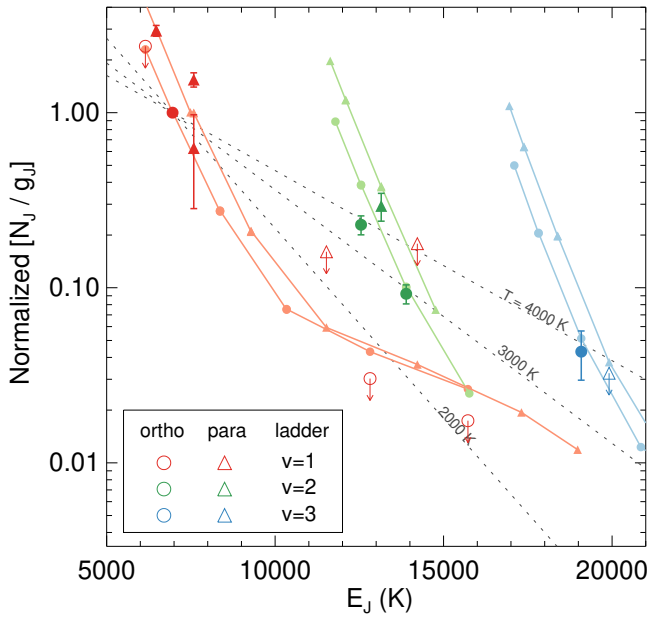


Figure 5. Excitation diagram of H₂ lines detected in G9.9–0.8. The y-axis is the column density ($N_{v,j}$) divided by the level degeneracy (g_j), and is normalized by that of the H₂ 1–0 S(1) line. The symbols with a downward-pointing arrow denote 3σ upper limits. The dashed lines represent the Boltzmann distribution with $T = 2000, 3000,$ and 4000 K. The solid lines represent the level populations expected from a warm, diffuse PDR with a significant contribution from collisional excitation (i.e., the “bh3d” model of [Draine & Bertoldi 1996](#) with $n_{\text{H}} = 10^2 \text{ cm}^{-3}$, $\chi = 10$, and $T_0 = 1000$ K, where χ is a parameter characterizing the UV intensity and T_0 is the temperature at the PDR boundary).

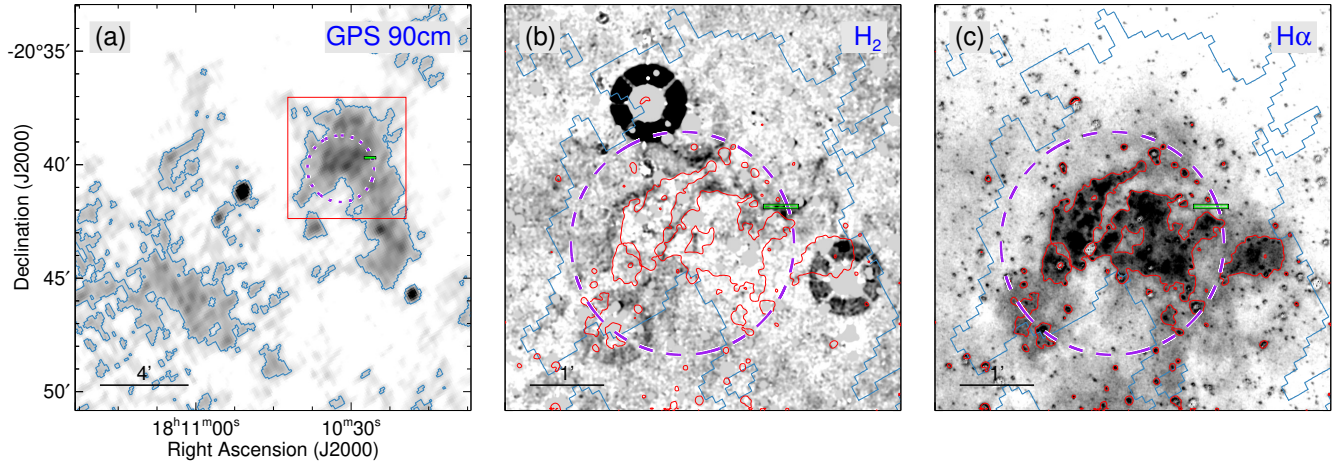


Figure 6. Multiwavelength images of G9.9–0.8: (a) radio continuum taken from the VLA 90 cm Galactic Plane Survey (GPS 90 cm; Helfand et al. 2006), (b) continuum-subtracted H_2 2.122 μm from the UWISH2 survey (Froebrich et al. 2011; Lee et al. 2019), and (c) continuum-subtracted $H\alpha$ images taken from the SuperCOSMOS $H\alpha$ Survey (SHS; Parker et al. 2005; Stupar & Parker 2011). The gray scales of the three images are linear. The red box in panel (a) marks the field of view of panels (b) and (c). The blue contours in panels (a)–(c) and the red contours in panels (b)–(c) represent the 90 cm continuum and $H\alpha$ emission features, respectively. The location of the H II region G9.982–0.752 identified by Lockman (1989) is marked by a purple circle, where the size of the circle corresponds to the half-power beam width of his radio observation ($\sim 3'$). The green horizontal bar represents the slit position of our NIR spectroscopy. The bar is made longer than the true slit length ($15''$) for display purposes.

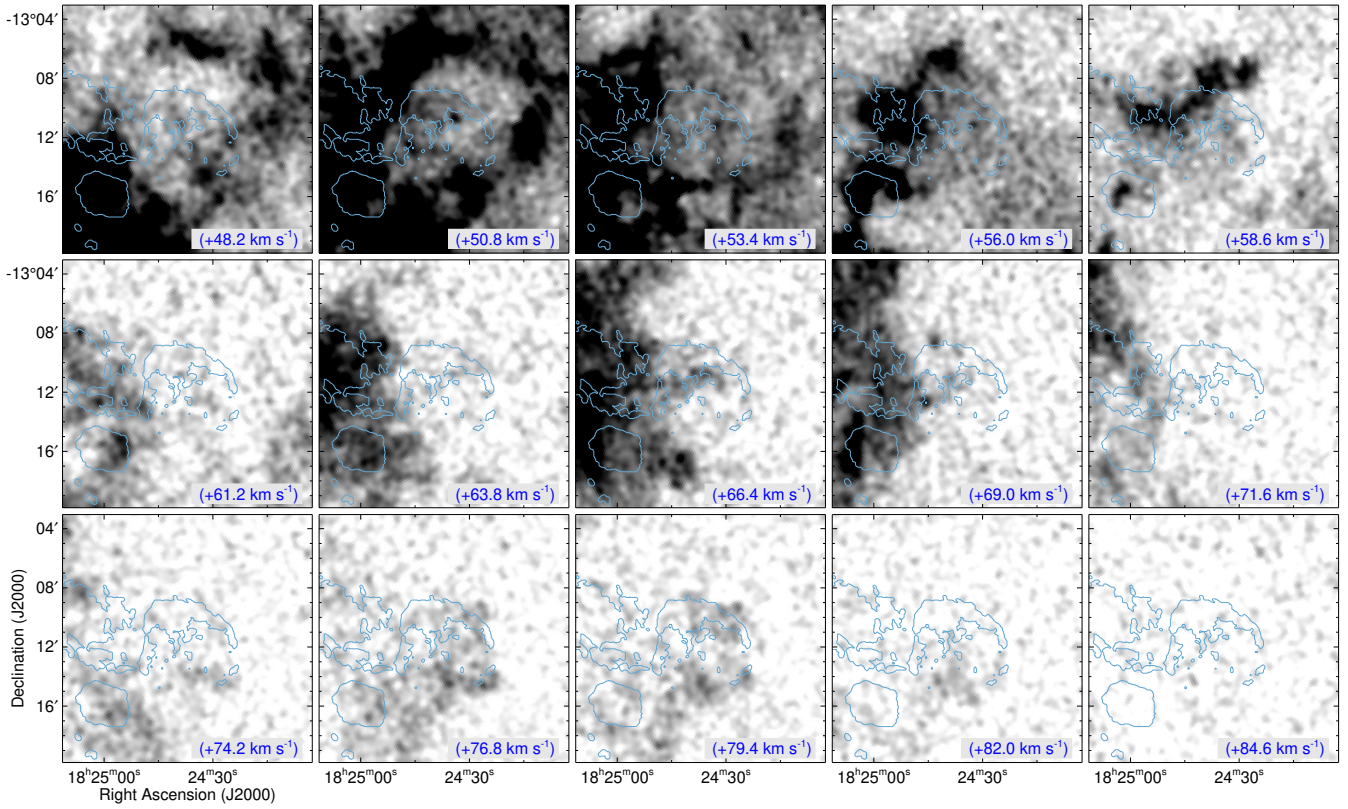


Figure 7. $^{12}\text{CO } J=1-0$ channel maps of G18.1-0.1 in the velocity range of +48–+85 km s^{-1} . Each channel map has been obtained by integrating over 2.6 km s^{-1} . The color scale is linear with the low and high thresholds of 0 and 90 K km s^{-1} , respectively. The blue contour represents the boundary of the remnant in 20 cm continuum (see Figure 1).

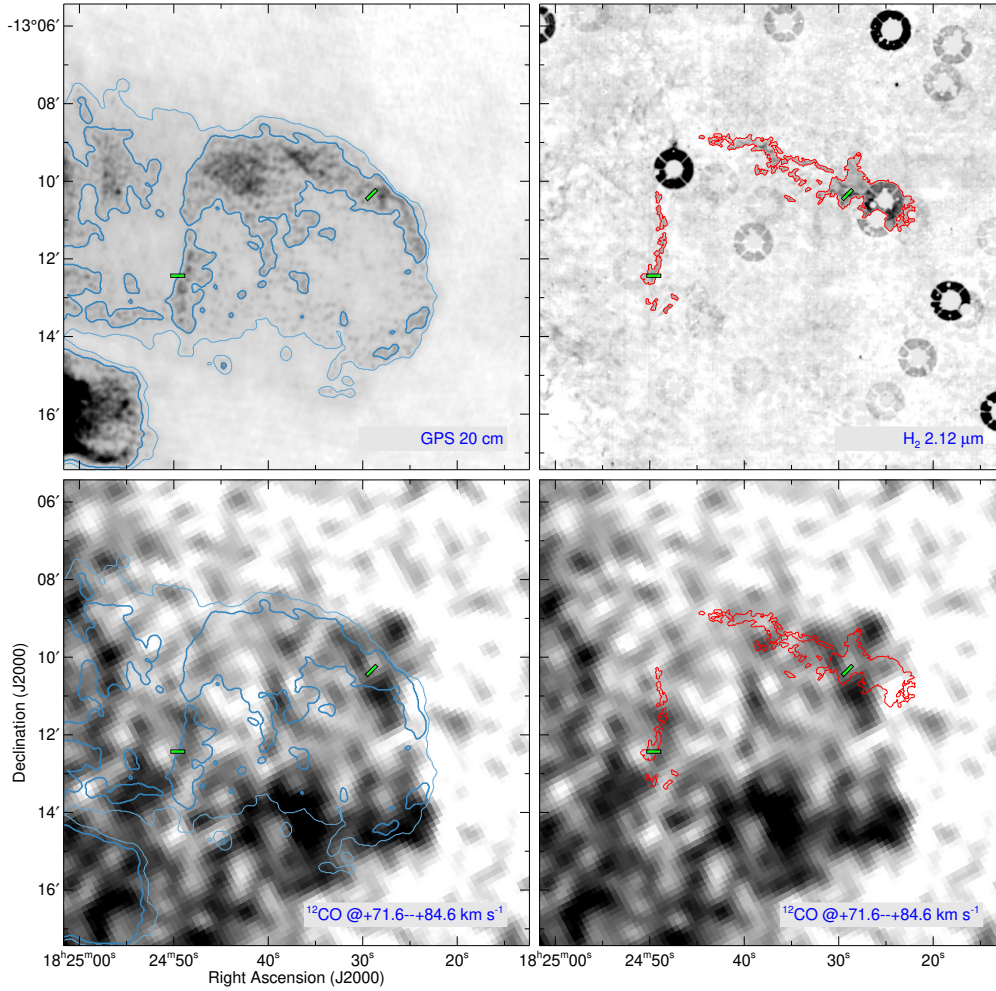


Figure 8. Top: 20 cm continuum and H_2 2.122 μm narrowband images of G18.1–0.1. The blue and red contours show the appearance of the SNR in 20 cm continuum and H_2 emission, respectively. The contour levels in the radio continuum image are 1.8 and 2.6 mJy/beam. The green bars represent the slit positions of our NIR spectroscopy. Bottom: zoomed-in ^{12}CO $J = 1-0$ intensity maps of G18.1–0.1 integrated from +72 to +85 km s^{-1} . The color scale is linear with the low and high thresholds of 0 and 120 K km s^{-1} , respectively.

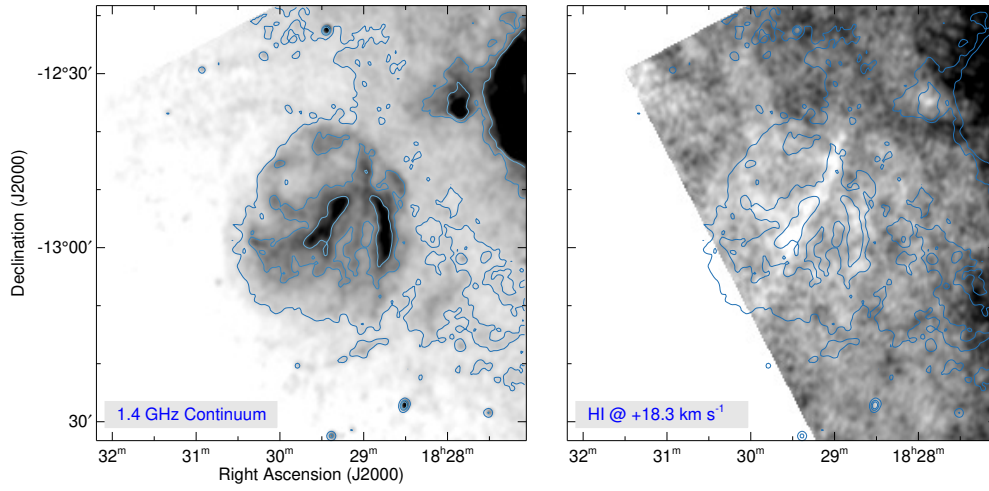


Figure 9. Left: 21 cm continuum image of G18.9–1.1. The color scale is linear with the low and high thresholds of 12 and 30 K, respectively. Right: H I 21 cm line channel map at $v_{\text{LSR}} = +18.3 \text{ km s}^{-1}$. The color scale is linear with the low and high thresholds of 50 and 110 K, respectively. The blue contours show the appearance of the SNR in 21 cm continuum, and the contour levels are 15, 20, and 25 K.

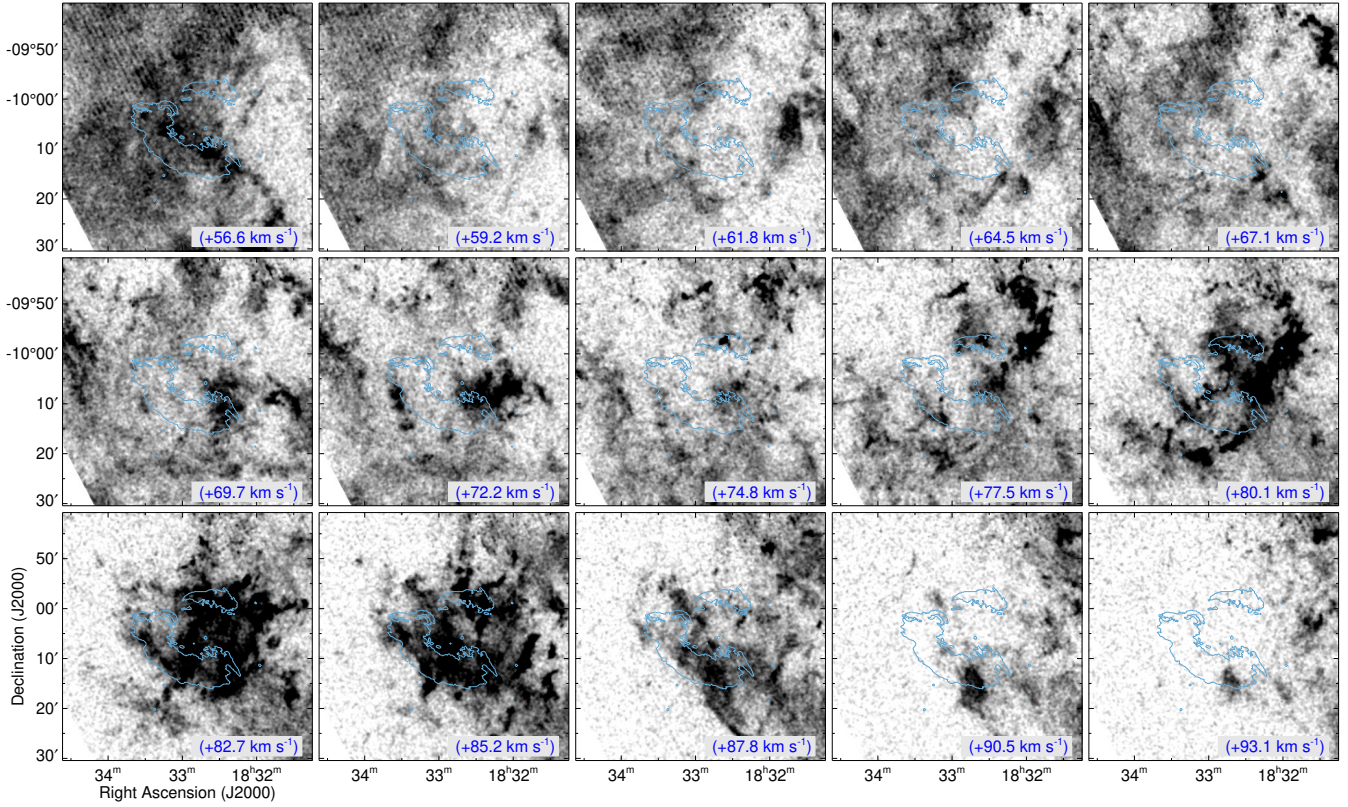


Figure 10. $^{12}\text{CO } J=1-0$ channel maps of Kes 69 in the velocity range of $+57$ – $+93 \text{ km s}^{-1}$. Each channel map has been obtained by integrating over 2.6 km s^{-1} . The color scale is linear with the low and high thresholds of 0 and 60 K km s^{-1} , respectively. The blue contour represents the boundary of the remnant in 20 cm continuum (see Figure 1).

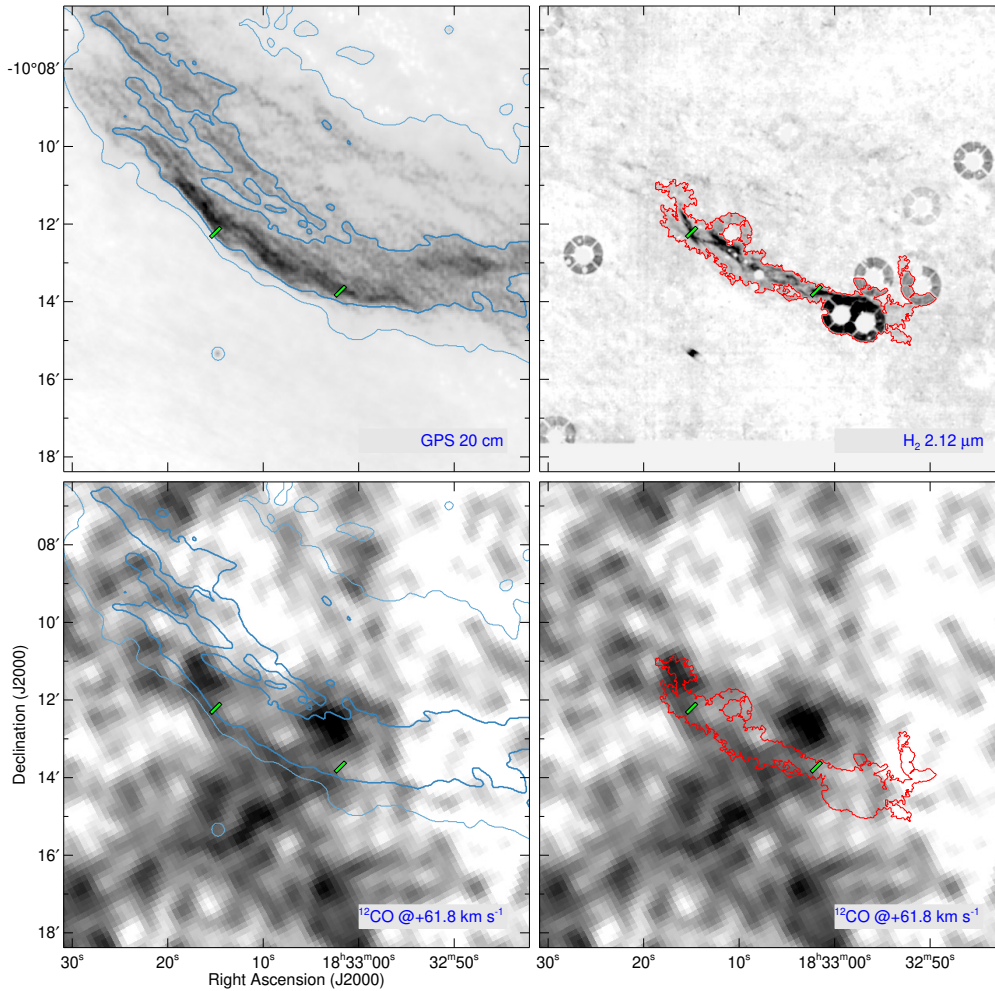


Figure 11. Top: 20 cm continuum and H₂ 2.122 μm narrowband images of Kes 69. The blue and red contours show the appearance of the SNR in 20 cm continuum and H₂ emission of the SNR, respectively. The contour levels in the radio continuum image are 2 and 6 mJy/beam. The green bars represent the slit positions of our NIR spectroscopy. Bottom: zoomed-in ¹²CO $J = 1-0$ channel map of Kes 69 at +62 km s^{-1} . The color scales are linear, and the low and high thresholds are 10 and 50 K km s^{-1} , respectively.

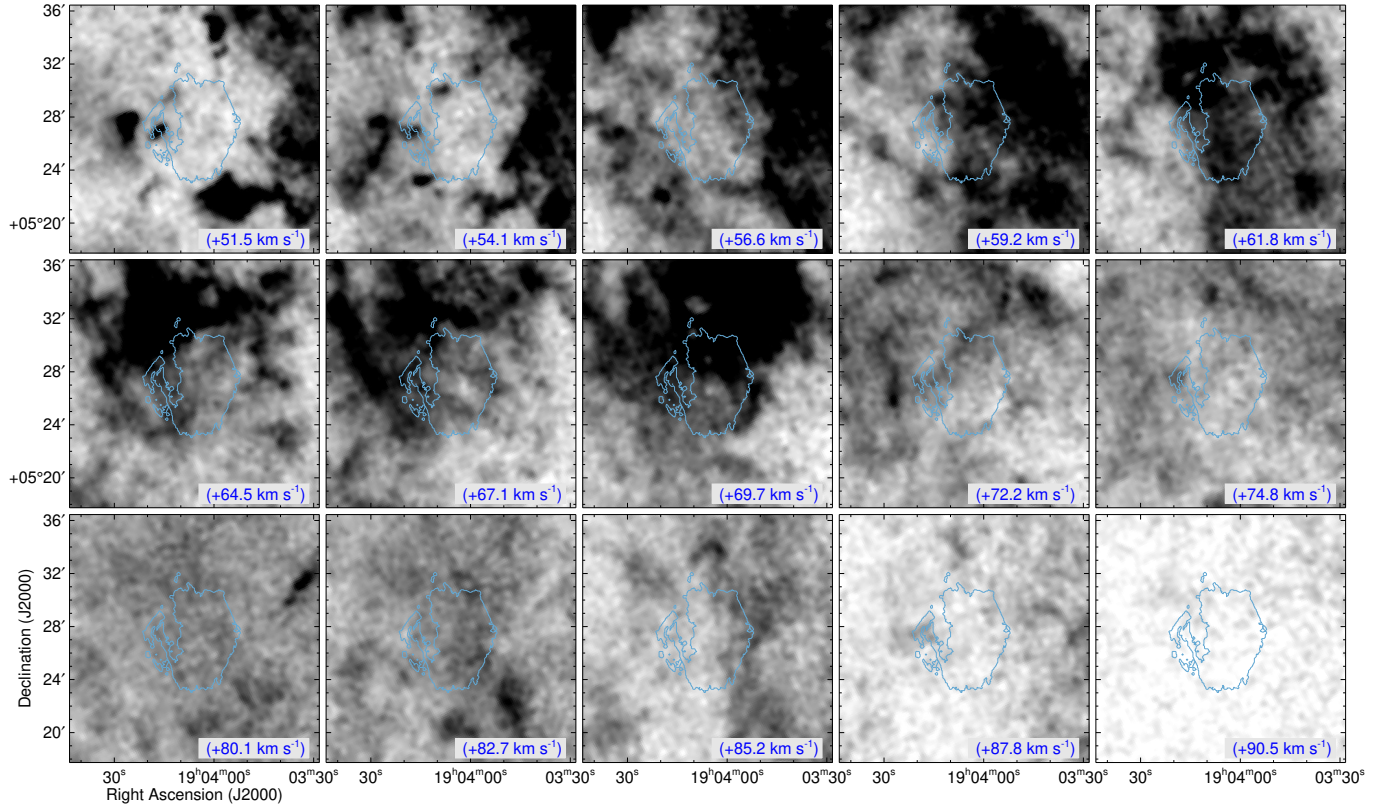


Figure 12. $^{12}\text{CO } J = 1-0$ channel maps of 3C 396 in a velocity range of $+52$ – $+91 \text{ km s}^{-1}$. Each channel map has been obtained by integrating over 2.6 km s^{-1} . The color scales are linear, and the low and high thresholds are 0 and 60 K km s^{-1} , respectively. The blue contour shows the appearance of the SNR in 20 cm continuum (see Figure 1).

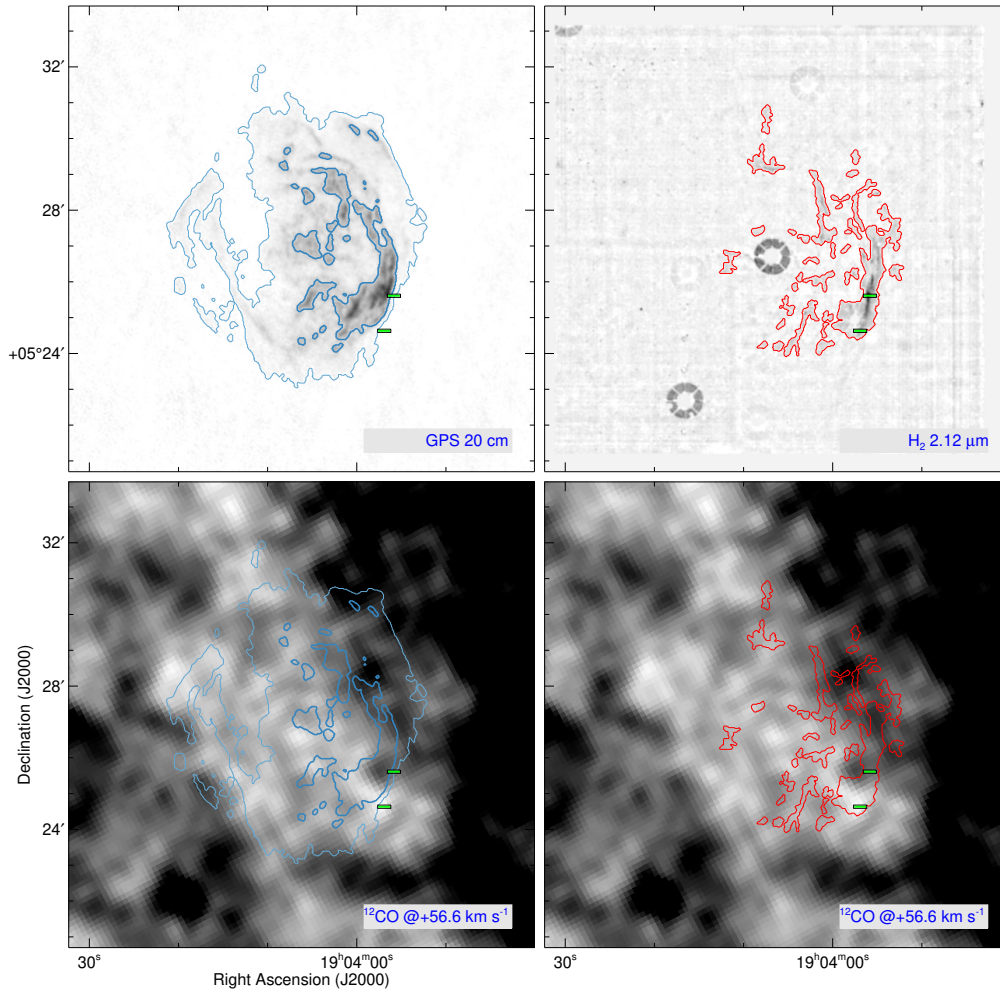


Figure 13. Top: 20 cm continuum and H₂ 2.122 μm narrowband images of 3C 396. The blue and red contours show the appearance of the SNR in 20 cm continuum and H₂ emission of the SNR, respectively. The contour levels in the radio continuum image are 0.3 and 3.0 mJy/beam. The green bars represent the slit positions of our NIR spectroscopy. Bottom: zoomed-in ¹²CO $J = 1-0$ channel map of 3C 396 at +56.6 km s⁻¹. The color scales are linear, and the low and high thresholds are 10 and 50 K km s⁻¹, respectively.

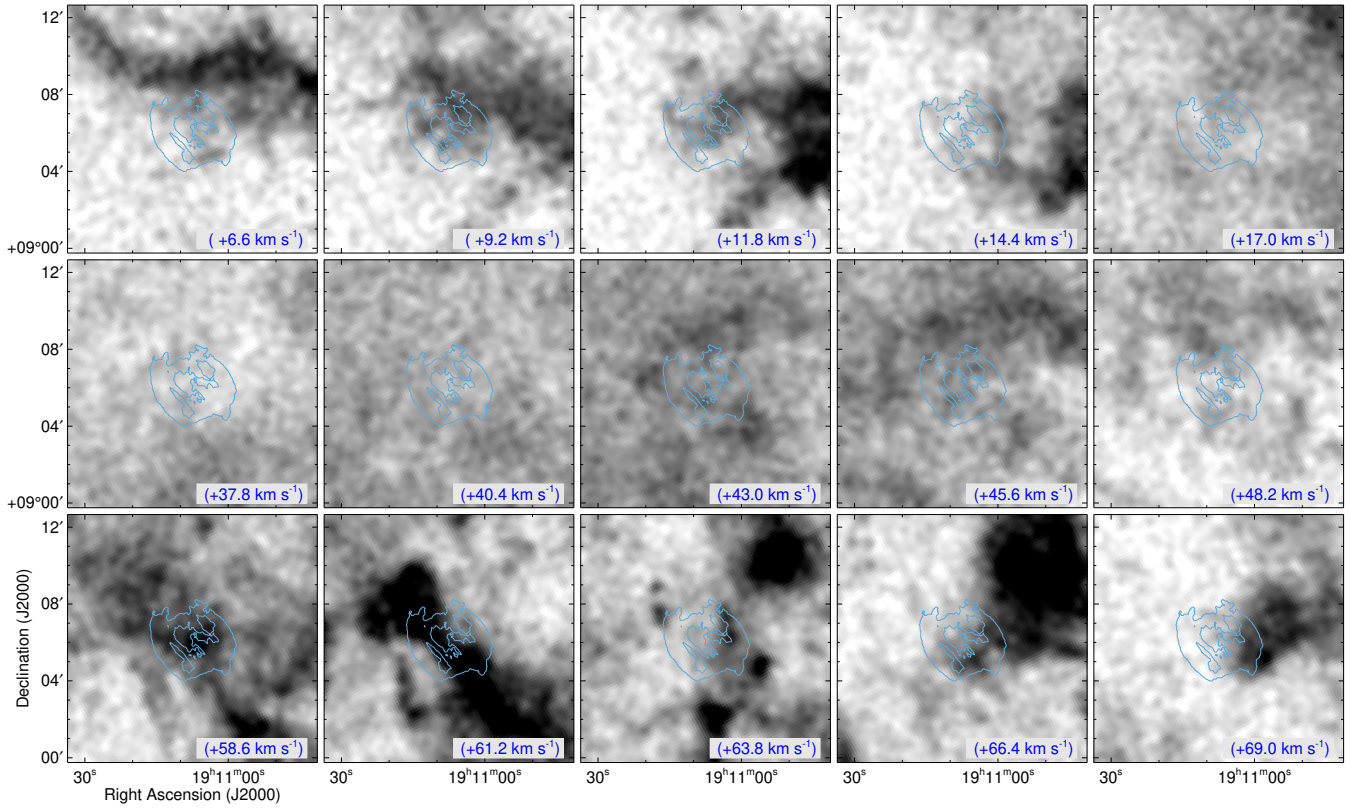


Figure 14. $^{12}\text{CO } J = 1-0$ channel maps of W49B in three different velocity ranges: $+7-+17 \text{ km s}^{-1}$ (top), $+38-+48 \text{ km s}^{-1}$ (middle), and $+59-+69 \text{ km s}^{-1}$ (bottom). Each channel map has been obtained by integrating over 2.6 km s^{-1} . The color scales are linear, and the low and high thresholds are 0 and 80 K km s^{-1} , respectively. The blue contour shows the appearance of the SNR in 20 cm continuum (see Figure 1).

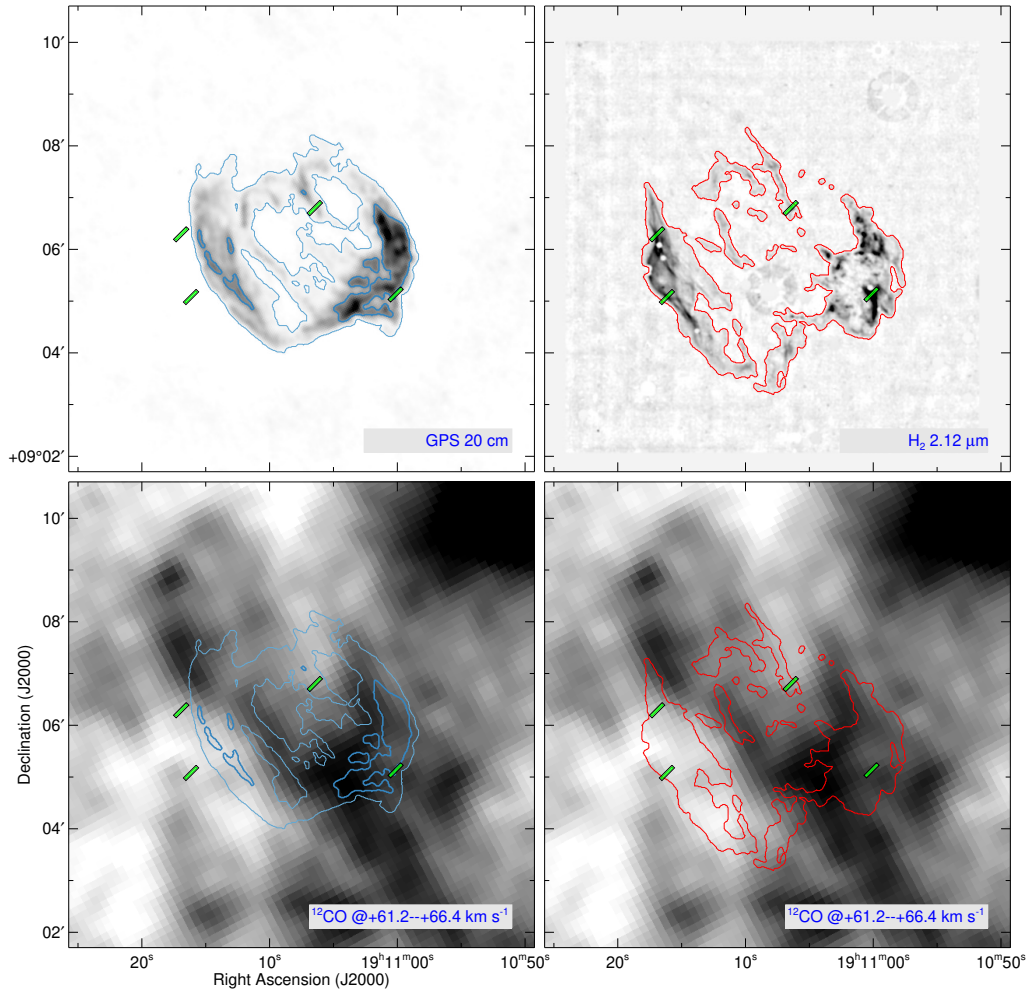


Figure 15. Top: 20 cm continuum and H₂ 2.122 μm narrowband images of W49B. The blue and red contours show the appearance of the SNR in 20 cm continuum and H₂ emission of the SNR, respectively. The contour levels in the radio continuum image are 3 and 30 mJy/beam. The green bars represent the slit positions of our NIR spectroscopy. Bottom: zoomed-in ¹²CO $J = 1-0$ intensity map of W49B integrated from +61 to +66 km s⁻¹. The color scales are linear, and the low and high thresholds are 40 and 200 K km s⁻¹, respectively.